# Carrier relaxation, pseudogap, and superconducting gap in high-$T_c$ cuprates: A Raman scattering study

M. Opel, R. Nemetschek, C. Hoffmann, R. Philipp, P. F. Müller, and R. Hackl
*Walther Meissner Institut, Bayerische Akademie der Wissenschaften, D-85748 Garching, Germany*

I. Tüttő
*Research Institute for Solid State Physics and Optics, P.O. Box 49, H-1525 Budapest, Hungary*

A. Erb, B. Revaz, and E. Walker
*DPMC, Université de Genève, CH-1211 Genève, Switzerland*

H. Berger and L. Forró
*EPFL, Ecublens, CH-1015 Lausanne, Switzerland*
(Received 27 July 1999)

We describe the results of electronic Raman-scattering experiments in differently doped single crystals of $YBa_2Cu_3O_{6+x}$ and $Bi_2Sr_2(Ca_xY_{1-x})Cu_2O_8$. The data in antiferromagnetic insulating samples suggest that at least the low-energy parts of the spectra of metallic samples originate predominantly from excitations of free carriers. We therefore propose an analysis of the data in terms of a memory function approach which has been introduced earlier for the current response. Dynamical scattering rates $\Gamma(\omega)=1/\tau(\omega)$ and mass-enhancement factors $1+\lambda(\omega)=m^*(\omega)/m$ of the carriers are obtained. It is found that a strong polarization dependence of the carrier lifetime develops towards low doping. In $B_{2g}$ $(xy)$ symmetry selecting predominantly electrons with momenta along the diagonals of the $CuO_2$ planes the Raman data compare well with the results obtained from dc and dynamical transport. In $B_{1g}$ $(x^2-y^2)$ symmetry projecting out momenta along the Cu-O bonds the dc scattering rates of underdoped materials become temperature independent and considerably larger than in $B_{2g}$ symmetry. This increasing anisotropy is accompanied by a loss of spectral weight in $B_{2g}$ symmetry in the range between the superconducting transition at $T_c$ and a characteristic temperature $T^*$ of the order of room temperature which compares well with the pseudogap temperature found in other experiments. The energy range affected by the pseudogap is doping and temperature independent. The integrated spectral loss is approximately 25% in underdoped samples and becomes much weaker towards higher carrier concentration. In underdoped samples, superconductivity-related features in the spectra can be observed only in $B_{2g}$ symmetry. The peak frequencies scale with $T_c$. We do not find a direct relation between the pseudogap and the superconducting gap.

## I. INTRODUCTION

Cuprate systems show a unique doping-temperature phase diagram, and the normal metallic (NC) and superconducting (SC) phases evolve from an antiferromagnetic (AF) insulating one upon increasing carrier concentration. For a wide doping range AF fluctuations are observed in the NC and SC states.[1–3] Especially at low doping, the normal state does not behave like a simple metal, and two if not three temperature ranges with qualitatively different properties have been identified below some 500 K.[4]

One of these ranges exists between the superconducting transition $T_c$ and a temperature $T^*$ and is characterized by the opening of a pseudogap which is well pronounced in the underdoped part of the phase diagram and disappears in overdoped samples. [2,5–13] Although the phenomenon has been investigated with various methods, the critical doping for its disappearance is not clear at the moment. Considering its origin several aspects have been discussed without, however, leading to a generally accepted picture. There are two main directions: (i) The pseudogap $\Delta^*$ is a precursor of superconductivity. Its characteristic energy is then expected to scale with the magnitude of the superconducting gap $\Delta$, and its momentum dependence should exhibit the same symmetry properties.[10,11,14–19] (ii) The pseudogap is a signature of the electronic interactions above $T_c$ but is not directly related to the SC pairing correlations. Then it can show independent scaling behavior and energy scales.[4,8,20] This means that the relationship between the pseudogap and the superconducting gap and its evolution with doping is of particular importance for the understanding of the cuprates.

The underdoped range of the phase diagram is remarkable not only because of the pseudogap but also for the increasing anisotropy of the carrier properties in the normal state. This is consistently observed in **k**-sensitive experiments such as angle-resolved photoemission spectroscopy[21] (ARPES) and electronic Raman scattering[22,23] (ERS) even if the details of the interpretation are not completely clear yet. In order to understand the anisotropy momentum-dependent electronic interactions are being considered. AF fluctuations, for instance, could lead to the observed characteristics as they are strong at low doping and tend to disappear somewhere in the so-called overdoped range. In an oversimplified but intuitive way the momentum dependence emerges directly if one recalls that nearest- and next-nearest-neighbor spins are ordered in an AF and ferromagnetic way, respectively, in an AF lattice. This basic idea and physically more elaborate versions of it have been worked out in some detail.[24,25] At

 

the same time the microscopic foundations such as Hubbard and $t$-$J$ models have been studied intensively.[26–29] The nesting properties of the Fermi surface can also lead to the observed phenomenology.[30]

In the present situation it is not only important to compare theoretical predictions and experimental results but also to relate results from different experiments to each other. Starting from a microscopical model the respective response functions can be calculated directly. In the case of Raman scattering a modified density response function is to be determined which has been done explicitly only for a few special cases.[25,30,31] However, the calculations become increasingly complicated along with the complexity of the electronic interactions studied. On the other hand, a more or less quantitative comparison of the results of different experiments is practically impossible in this way. Therefore, it seems worthwhile to derive more commonly used functions from the spectra instead. Such a procedure is standard in infrared (IR) or optical spectroscopy. There, apart from the conductivity, particle lifetimes $\tau(\omega,T)$ or scattering rates $\Gamma = 1/\tau$ and mass-enhancement factors $1+\lambda(\omega,T) = m^*(\omega,T)/m_b$ with $m_b$ the band mass are derived from the reflectivity[32] following the relaxation or memory function approach proposed by Götze and Wölfle.[33] We will demonstrate in detail below that the method can be adapted for the analysis of the ERS data. We will apply it to our results and utilize it even beyond a simple comparison of results from various experiments. It is important to note, however, that the different methods cannot be expected to return identical results for the quantities under consideration as they measure different correlation functions. The interaction between a system and a certain experimental probe is described by the vertex which can well have a nontrivial dependence on energy, for example, due to renormalization,[34] and influence the response considerably. IR and Raman scattering are two-particle excitations being (essentially) described by current-like and density-like response functions. In most of the cases the vertices can be expressed to a good approximation in terms of the one-electron energies in the conduction band $\epsilon(\mathbf{k})$ as $j_\alpha \propto \partial\epsilon(\mathbf{k})/\partial\mathbf{k}_\alpha$ and $\gamma(\mathbf{k}) \propto \partial^2\epsilon(\mathbf{k})/\partial\mathbf{k}_\alpha\partial\mathbf{k}_\beta$, respectively. ARPES and electron tunneling spectra reflect the response of single-particle excitations. Therefore, only a qualitative comparison can be achieved. Nevertheless, a better understanding of the interrelation of the different experimental methods is very useful as they are complementary in many senses. They couple, for instance, to different excitations and have different energy and momentum resolutions. A similar step in the direction we want to pursue here for Raman scattering has recently been accomplished for the ARPES data in that the electron self-energy $\Sigma(\mathbf{k},\omega)$ has been derived.[35]

In ERS the energy resolution is fairly good and there is also a limited momentum resolution. In addition, the density-like coherence factors in the superconducting state allow one to clearly distinguish between the occurrence of a gap and of phase coherence among the pairs. This leads to qualitatively new conclusions in the analysis of the SC gap and the pseudogap. The momentum resolution has its origin in the $\mathbf{k}$ dependence of the Raman vertex $\gamma_\mathbf{k}$ which depends on the polarizations of the incoming and scattered photons $\mathbf{e}^I$ and $\mathbf{e}^S$ and, in the most general case, on the full band structure $\epsilon_n(\mathbf{k})$. As outlined above $\gamma_\mathbf{k}$ is often approximated by the second derivative of the conduction band contracted with the polarization vectors (effective-mass approximation). In any case, $\gamma_\mathbf{k}$ can be decomposed into its symmetry components $\Phi_L^\mu(\mathbf{k})$ where $L$ denotes the order of expansion and where the symmetry is indexed by $\mu = B_{1g}$, $B_{2g}$, $A_{1g}$, and $A_{2g}$. As the symmetries correspond to certain light polarizations a relation between momentum and configuration space is established which allows one to weigh out different parts of the Fermi surface or of the Brillouin zone with different polarization combinations.[36–38] Using this $\mathbf{k}$ resolution of ERS the anisotropy of the superconducting gap $\Delta(\mathbf{k})$ has been studied in the cuprates.[36]

Normal-state anisotropies were already inferred from ERS results a while ago[22] without, however, mapping them onto $\mathbf{k}$ space. The static lifetime as obtained from the Raman spectra was compared to ordinary transport.[39] More recently, we have investigated normal-state anisotropies systematically for different doping levels in Bi- and Y-based compounds.[23] For momenta along the principal axes (parallel to the Cu-O bonds in the planes) as opposed to those parallel to the diagonals the quasiparticle lifetimes in the static limit ($\omega = 0$) seem to become extremely short in underdoped, still metallic, and SC samples. In contrast, there is almost no anisotropy in the overdoped range. Independent of doping the ERS data at $B_{2g}$ symmetry compare well with ordinary transport.[23]

One purpose of the present paper is to extend the study to finite energies and to derive dynamical scattering rates from the Raman data. The range $\omega \neq 0$ must be analyzed with even more care than the dc limit since in a Raman experiment coupling to almost all excitations in a solid is possible. For a derivation of the carrier dynamics other contributions such as phonons or magnons must therefore be identified and eventually be subtracted. Fortunately, selection rules and resonance studies using various energies for excitation allow a relatively safe distinction. Nevertheless, we do not think we are already in a position to subtract contributions coming from other than carrier excitations. We rather realize that carrier excitations dominate at low energies and will therefore confine ourselves to the range up to 1000 $\mathrm{cm}^{-1}$. The method for the determination of dynamical properties will be derived in detail. We show that the influence of energies larger than 1000 $\mathrm{cm}^{-1}$ leads only to logarithmically small corrections. The data for the scattering rate and the mass renormalization will be compared to the IR results. In addition, we will calculate reflectivities for a few examples. A careful study of the dynamical response as a function of temperature allows us also to better understand the pseudogap state. As a result, we can extrapolate the normal-state behavior observed at $T > T^*$ to the range between $T^*$ and $T_c$ and obtain a better estimate of the full influence of the pseudogap on the spectra as a function of temperature and doping. This, finally, leads to a comparison of superconducting and pseudogap states. We find clear indications for two different energy scales.

The paper is organized as follows: In Secs. II and III details of the samples and of the experiment, respectively, will be described. The experimental results are compiled in Sec. IV where we focus on raw data only. The analysis in terms of the memory function will be summarized in Sec.

V A and described in more detail in the Appendix. In Sec. V B dynamical scattering rates and mass renormalization factors will be derived from the data presented in Sec. IV using the method described in Sec. V A. The discussion (Sec. VI) is split into four subsections. In Sec. VI A the derived quantities will be analyzed with respect to their low-frequency limits and to their symmetry dependence. They will be compared to results from other methods, specifically optical transport, in Sec. VI B. The pseudogap and its relation to the superconducting gap will be discussed in detail in Secs. VI C and VI D, respectively. We present data for two groups of compounds and at least four doping levels for each one. The implications will be summarized in Sec. VII.

## II. SAMPLES

The $YBa_2Cu_3O_{6+x}$ (Y123) crystals were grown in $BaZrO_3$ crucibles.[40,41] $BaZrO_3$ has been shown to be completely inert and to facilitate the preparation of samples with a purity of better than 99.995%. All crystals were postannealed in pure oxygen and quenched. Temperatures and oxygen partial pressures were adjusted according to the calibration of Lindemer *et al.*[42] The resulting oxygen concentrations were approximately 6.1, 6.5, 6.93, and very close to 7.0 for the samples we call AF insulating, underdoped, optimally doped, and overdoped, respectively, in the following. The determination of the doping level through the annealing conditions proved to be extremely reliable in Y123 with stoichiometric cation composition. Using nondestructive methods the oxygen concentration cannot be measured as precisely. There exists a relationship between the oxygen doping and the position of the Raman-active vibration of the apex oxygen along the *c* axis.[43] For the metallic samples we obtained 6.53, 6.93, and 6.96. Given the uncertainty of the Raman-based determination of approximately $\pm 0.05$ the results must be considered consistent, and they show independently that the oxygen content in the surface layer studied is close or identical to the nominal one. In the AF sample the phonon could not be observed for the polarizations studied. The magnetically determined respective $T_c$ values (midpoints) and transition widths (10%–90%) of the superconducting samples were 53.5 K ($\Delta T_c = 3$ K), 91.5 K ($\Delta T_c = 0.3$ K), and 87.0 K ($\Delta T_c = 1.0$ K). The $T_c$ of the underdoped sample when being illuminated by the laser shifts up by several degrees. For the power and the exposure time used the saturation limit applies, and the actual $T_c$ is close to 60 K.[44]

The Bi-based samples $Bi_2Sr_2(Ca_xY_{1-x})Cu_2O_8$ (Bi2212) were prepared in ZrO crucibles. In crystals close to optimal doping (without Y or, equivalently, $x=1$ and appropriately adjusted oxygen content) the resistively measured $T_c$ was generally above 90 K with $\Delta T_c < 2$ K. According to transport and Raman results the sample with $T_c = 92$ K is slightly underdoped. If $Ca^{2+}$ is replaced by $Y^{3+}$, holes in the $CuO_2$ planes are filled in and $T_c$ is reduced. The samples we used contained 38% Y and 100% Y, respectively. The superconducting sample (38% Y) was well in the underdoped range of the phase diagram with a $T_c$ of 57 K ($\Delta T_c = 5$ K). Overdoping was achieved by annealing the crystals in oxygen at the appropriate partial pressure resulting in $T_c$'s of 81.6 K ($\Delta T_c = 0.5$ K) and 58 K ($\Delta T_c = 5$ K) for the samples we used. It has been shown for several compounds that $T_c$ depends in a unique way on the effective doping $p$ as $T_c = T_c^{\max}[1 - 82.6(p-0.16)^2]$.[45] This relation is used to determine the respective $p$'s from the transition temperatures. Given the uncertainty in $T_c$ and $T_c^{\max}$ the typical error for the doping is $\Delta p = 0.01$. The doping levels $p$ for our (SC) samples are then 0.09 ($T_c = 57$ K), 0.15 ($T_c = 92$ K), 0.16 ($T_c = 90$ K), 0.19 ($T_c = 81.6$ K), and 0.23 ($T_c = 58$ K). The doping level of the AF sample is close to zero but has not been determined independently. The $T_c$ of the sample we call optimally doped is smaller than that of the slightly underdoped one due to a higher degree of disorder. The increase with time of the maximally obtainable $T_c$ is a generally observed phenomenon which can be traced back to an improved crystallographic structure and higher purity. Therefore the samples are sometimes classified in ''generations.'' In this nomenclature the optimally doped sample comes from the second generation ($T_c^{\max} \simeq 90$ K) while the slightly underdoped one is out of the third generation ($T_c^{\max} \simeq 93$ K).

Bi2212 is not stable at the stoichiometric composition and there is always excess Bi in the crystals (typically $Bi_{2.1}$ instead of $Bi_2$),[46,47] which is found predominantly in the Ca (Y) position. In addition, a small amount of Sr may be replaced by Ca or Y. In general, it cannot be expected for Bi2212 that a crystal quality comparable to the one of Y123 is obtainable. By partially substituting Bi with Pb the modulation along the crystallographic *b* axis can be changed or even suppressed completely.[48] In the sample we used, the Laue pattern still showed an indication of a twofold symmetry but it is reasonable to assume that the distortion is smaller than in Pb-free samples. If the doping is changed by varying the oxygen content, the ratio of the metal atoms plays a crucial role for the stability, and underdoped material may become unstable and disintegrate.

## III. EXPERIMENT

The experiments were performed in pseudo backscattering geometry with an angle of incidence close to 65° and the sample surface perpendicular to the crystallographic *c* axis. Due to the large real part of the refractive index ($n \simeq 2$), the light propagates almost parallel to the *c* axis inside of the sample. For the analysis of the scattered light we used a double monochromator with single-channel detection. For constant slit width the resolution depends on the wavelength of the scattered light. The slits were set at 550 $\mu$m; hence the spectral resolution is approximately 10, 6, and 3 $cm^{-1}$ in the violet, the green, and the red range of the spectrum, respectively. All spectra are given in units of photon counts per second (cps) and are proportional to the cross section. They are corrected for the sensitivity of the instrument but not for the frequency dependence of the optical constants. However, $n$ and $k$ do not change by more than a few percent in the region of interest.[49] For excitation an $Ar^+$ laser was used, and for most of the experiments the line at 458 nm was selected. In a few cases the lines at 476 and 514 nm were used. In order to keep the laser-induced heating low ($5\ \text{K} < \Delta T < 15$ K typically) the power was set between 1 and 4 mW depending on the thermal conductivity of the sample. The actual $\Delta T$ and hence the spot temperature were determined in any individual case via the ratio of the Stokes to the

anti-Stokes intensity. Energy gain and loss spectra fit very well. Therefore, in addition to a well-defined measuring temperature, we have strong experimental support for the fluctuation-dissipation theorem to apply. The beam was focused to a spot of approximately $50\times150$ $\mu m^2$. The polarizations of the incoming and outgoing photons were always parallel to the planes. The coordinate system is locked to the Cu-O bonds with $x=[100]$, $x'=[110]$, etc. All symmetries refer to a tetragonal point group. $B_{1g}$ and $B_{2g}$ excitations can be projected out separately with $x'y'$ and $xy$ polarizations, respectively. Excitations transforming as $A_{1g}$ cannot be accessed independently. All configurations with the incoming and the outgoing photon polarizations being parallel project out the $A_{1g}$ contribution with angle-dependent $B$ admixtures which have to be subtracted accordingly. Typically, one uses $xx-x'y'$ and $x'x'-xy$. As described in detail in other publications there exists a relationship between electronic momenta and light polarizations through the symmetry properties of the Raman vertex: At $B_{1g}$ and $B_{2g}$ symmetry electrons with momenta along the principal axes and the diagonals, respectively, are weighed out predominantly.[36] If one is interested in sorting out contributions which transform like $A_{2g}$ it is necessary to use circularly polarized light in addition to the linear polarizations.[50,51]

The samples are mounted on the cold finger of a He flow cryostat with the temperature adjustable between 1.5 and 330 K. The vacuum the sample surface is exposed to is pumped cryogenically and is better than $10^{-6}$ mbar. For removing surface layers accumulating at low temperature the sample is heated to 250 K once a week. Then the experimental conditions are stable and the spectra are fully reproducible. As a general feature in the cuprates the scattering intensity at $\hbar\omega\gg k_BT$ becomes constant. In Fig. 1 we plot the average intensity between 800 and 1000 $cm^{-1}$ (corresponding to 1100–1400 K). A variation within $\pm7\%$ of the mean value is found. Obviously, there is no systematic dependence on temperature. This is confirmed by linear regression analysis which produces the horizontal lines shown in the figures; they are not the ordinary average of the data. The statistical scatter of the data comes from several sources which cannot be controlled sufficiently including the influence of adsorbed surface layers. Since there is no trend, it is safe to assume that the overall sensitivity varies accordingly without exhibiting a spectral dependence. To correct for those small variations all spectra shown below are adjusted to the mean value by a multiplicative constant between 0.75 and 1.25.

## IV. RESULTS

Figure 2 shows a compilation of Raman results in Y123 at three doping levels, close to 6.0, 6.5, and 7.0. The pure symmetry components are plotted in order to specifically clarify the role of the $A_{1g}$ symmetry. As a consistency check the differences $xx-x'y'$ and $x'x'-xy$ can be compared. The observed phonon lines are in complete agreement with the published literature.[43,52] The high intensity ratio of the phonons to the continuum independently proves the very high crystal quality. The line at approximately 585 $cm^{-1}$ which is induced by disorder in the chains[43,52] is present in all samples, even in the undoped and the fully doped ones. This means that a few oxygen atoms are still missing in

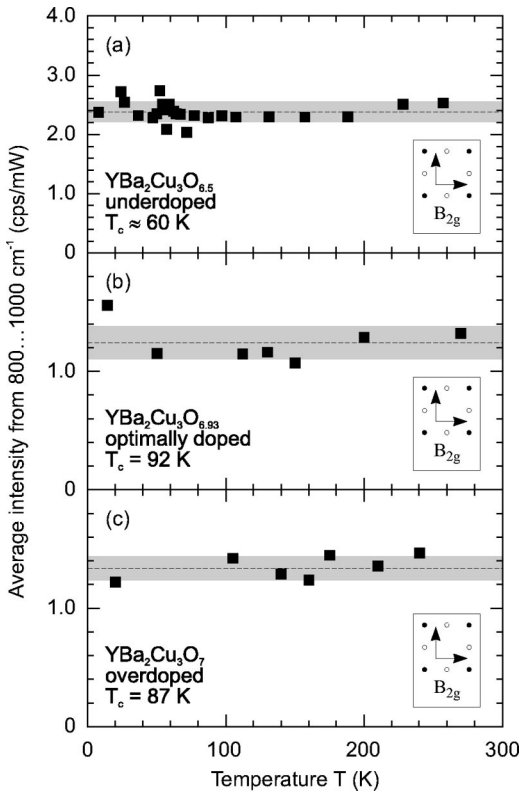


FIG. 1. Average intensities in the constant part of the spectra (800–1000 $cm^{-1}$) for differently doped Y123 at $B_{2g}$ symmetry as a function of temperature. The size of the dots approximately represents the statistical error. The shaded area is the variance of the average.

Y123(7.0) and some are left over in Y123(6.0).

There are several new features of the continuum which have not yet been shown or discussed in previous publications. Particular attention should be paid to the AF insulating sample [Figs. 2(a), 2(d), and 2(g)] where all intensities of the continuum are generally smaller than in the metallic crystals; the $B_{2g}$ intensity vanishes almost completely. At present it is not clear whether or not the residual 0.5 photon counts per second and mW are intrinsic or due to surface degradation or contamination. A similar intensity is also found in the superconducting state at very low frequency at all doping levels (see Fig. 7 below). The cross section at $B_{1g}$ symmetry is higher by a factor of 3, but once again approximately the same residual intensity is found in superconducting samples close to optimal doping (see Ref. 53). It seems, however, qualitatively clear that at least the $B_{2g}$ intensity is very close to zero in undoped samples. This is plausible since the $B_{2g}$ channel apparently samples the carriers at all doping levels studied.[8,9,23] The intensities we found for the undoped sample are also considerably smaller than those observed by Katsufuji *et al.*[54] for comparable $La_{2-x}Sr_xCuO_4$ (LSCO). The difference between Y123(6.5) and Y123(7.0) is, to within the experimental error, the same as already found earlier by Chen and co-workers.[55]

To make things more quantitative we will focus on those parts of the spectra which are not subject to trivial changes due to the thermal Bose-Einstein function, i.e., on the energy range $\hbar\omega\gg k_BT$. As demonstrated in the experimental section (Fig. 1) the intensity between 800 and 1000 $cm^{-1}$ does

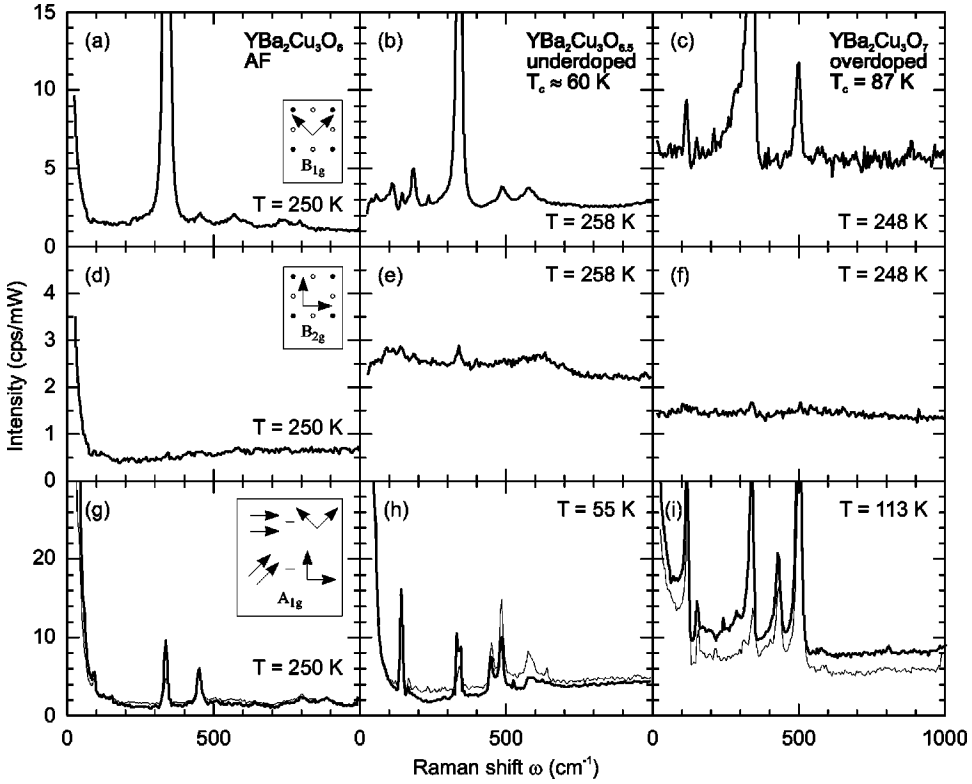


FIG. 2. Compilation of Raman results for Y123 at characteristic doping levels. Shown are the pure symmetries as indicated in the figure. In order to demonstrate the reliability of the subtraction procedure which is required to obtain pure $A_{1g}$ we show both $xx-x'y'$ and $x'x'-xy$. Except for the overdoped sample (i) with the strongest orthorhombic distortion the discrepancies are of the order of the experimental error. In the overdoped sample, although twinned, there is preferential orientation.

not depend on temperature below 300 K in a systematical fashion. For the study of the doping dependences of the intensities at the three main polarizations we will therefore compare the average scattering cross sections measured between 800 and 1000 $cm^{-1}$ (Fig. 3). The $B_{1g}$ intensity decreases continuously upon the reduction of carriers while a kind of kink is found for both $A_{1g}$ and $B_{2g}$ symmetry. Moreover, the $B_{2g}$ intensity is peaked at an oxygen content of 6.5 in Y123 [Fig. 3(a)] and close to optimal doping in Bi2212 [Fig. 3(b)]. In this context, it should be mentioned that the optical constants for visible light depend only weakly on doping,[49] and the internal cross section is expected to vary by less than a factor of 2 when changing the oxygen content from 6.0 to 7.0 in Y123. We did not correct the spectra for the change of the optical constants. Nevertheless, trivial effects such as an increase of the intensity on doping can be excluded as the variation of the cross section is monotonous only in the $B_{1g}$ symmetry but exhibits a maximum at $0.1<p<0.15$ for the $B_{2g}$ channel. If the $B_{1g}$ and the $B_{2g}$ intensities are added the doping dependence of the sum is very similar to that in $A_{1g}$ symmetry. This is noteworthy since at lowest order the variation of the magnitude of the $A_{1g}$ vertex on the Fermi surface resembles closely that of the sum of the $B_{1g}$ and $B_{2g}$ vertices. The results in Bi2212 are similar to those described for Y123. The advantage here is that we have also data for strong overdoping. The ratio of the $B_{1g}$ to the $B_{2g}$ intensity has been studied in great detail in LSCO by Naeini *et al.*[56] and is found to be in full agreement with the data presented here.

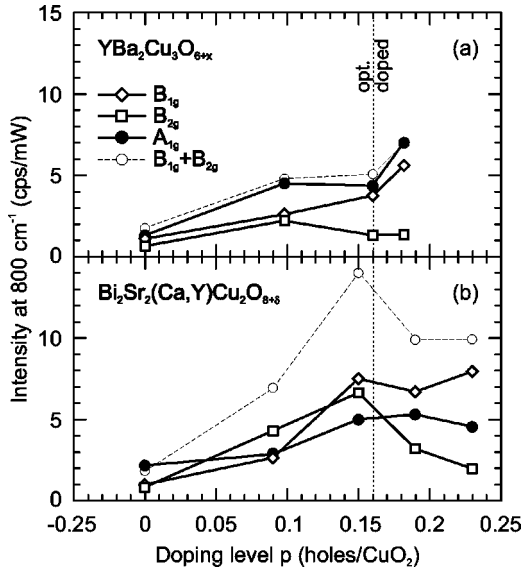


FIG. 3. Average intensities in the frequency- and temperature-independent part of the spectra (800–1000 $cm^{-1}$) for differently doped Y123 (a) and Bi2212 (b) as a function of symmetry. In Y123 (a), $A_{1g}$ is apparently the direct sum of $B_{1g}+B_{2g}$. The Bi2212 samples come from different sources and ''generations;'' hence there is more uncertainty in the data. The qualitative behavior such as the maximum in $B_{2g}$ symmetry is reproducible.

For a clarification of the nature of the excitations it is instructive to study an extended energy range. $B_{2g}$ spectra of differently doped Y123 are plotted in Fig. 4. As we have already seen in Fig. 2 the spectra are almost constant in the low-energy part. Between 1000 and 2000 $cm^{-1}$ the slope

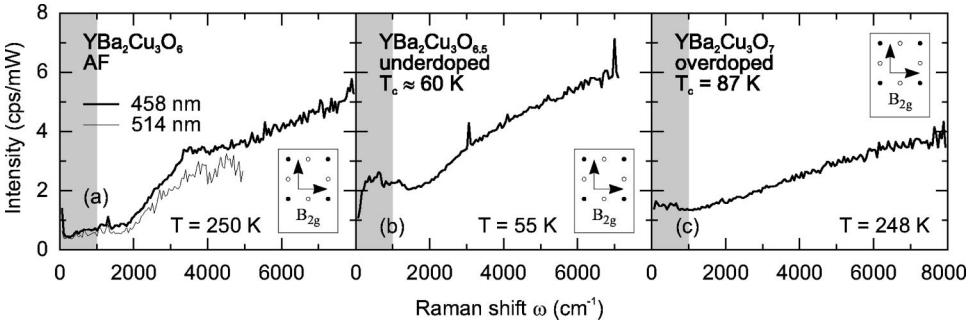


FIG. 4. $B_{2g}$ spectra for differently doped Y123 at large energy transfers.

changes and the cross section starts to increase substantially. The same trend is found for the $B_{1g}$ symmetry where scattering from two-magnon excitations is superimposed on the linear continuum at all doping levels.[1,57,58] In contrast, in $A_{1g}$ symmetry the intensity at high energy transfers decreases continuously and extrapolates to zero between 10 000 and 12 000 $cm^{-1}$ as already observed a while ago in $Gd_2CuO_4$.[50] Spectra for Y123(6.0) at energy transfers between 6000 and 15 000 $cm^{-1}$ show similar trends and, in addition, structures in the range between 1.5 and 1.8 eV (12 000 and 15 000 $cm^{-1}$).[51] The complete results we obtained at high energy transfers will be published elsewhere.

As already pointed out by Reznik and co-workers,[59] there is a relatively strong contribution to the cross section which is almost independent of doping. Here we find a well-resolvable gap for that excitation of some 1500 $cm^{-1}$ (200 meV) for Y123(6.0) and Y123(6.5) and one of the order of 1000 $cm^{-1}$ (150 meV) for Y123(7.0). Superimposed on this so far unidentified continuum (see, however, Ref. 51) there are contributions from scattering off carriers at energies down to zero, from spin excitations between 1000 and 4500 $cm^{-1}$ and, of course, from phonons in the range up to 800 $cm^{-1}$. The gapped continuum has $A_{2g}$ symmetry as it can be observed with comparable intensity at both $B_{1g}$ and $B_{2g}$ symmetries. This can be checked with circularly polarized light but will not be the subject of this publication. For a thorough understanding of inelastic light scattering in the cuprates the origin of all contributions must be clarified. It seems, however, safe to attribute the low-energy part of the $B_{2g}$ continuum to scattering from carriers as already shown earlier[8,23] and to neglect an interaction with other contributions such as spin excitations. In the following we will therefore assume the $B_{2g}$ continuum for energies below 1000 $cm^{-1}$ to consist of a single component. Apparently, the situation is more complicated in $B_{1g}$ symmetry where no superconductivity-induced features can be found at low doping.[8,9,23,55,56]

We turn now to the temperature dependence of the spectra and focus on the $B_{2g}$ response in metallic samples in the range $0.09<p<0.23$. In this context we have to recall that according to the fluctuation-dissipation theorem the Raman cross section and, consequently, the number of inelastically scattered photons registered per unit time, $\dot{N}_{\gamma\gamma}(\omega,T)$, are proportional to the imaginary part of the Raman response function $\chi_{\gamma\gamma}(\mathbf{q}\simeq 0,\omega,T)$,

$$\dot{N}_{\gamma\gamma}(\omega,T)=R_{\gamma\gamma}\{1+n_B(\omega,T)\}\chi''_{\gamma\gamma}(\mathbf{q}\simeq 0,\omega,T), \qquad (1)$$

where $\{1+n_B(\omega,T)\}$ is the Bose-Einstein function. The response function $\chi_{\gamma\gamma}(\omega)=\chi'_{\gamma\gamma}(\omega)+i\chi''_{\gamma\gamma}(\omega)$ for inelastic scattering of light from electrons in metals is equivalent to a correlation function of the effective density[60] and is strongly polarization dependent through the vertex $\gamma$. To a very good approximation we can take the limit of zero momentum

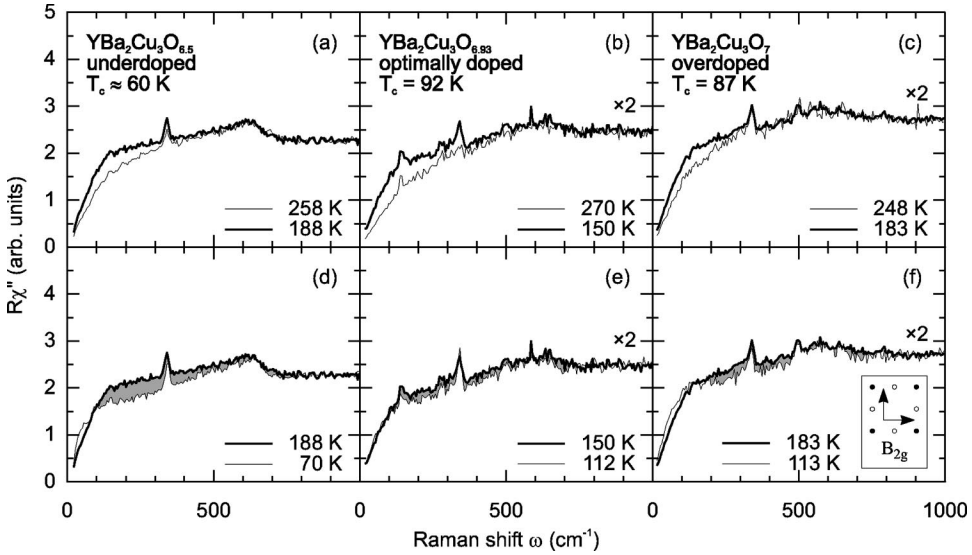


FIG. 5. $B_{2g}$ spectra for Y123 at different doping levels as indicated for $T>T_c$. The upper panels (a)–(c) show spectra at $T>T^*$. In the lower ones (d)–(f) spectra close to $T_c<T^*$ are compared to those at $T\simeq T^*$. For clarity the spectra of the optimally doped (b),(e) and the overdoped (c),(f) samples have been multiplied by a factor of 2. The shaded areas indicate the anomalous loss of spectral weight.

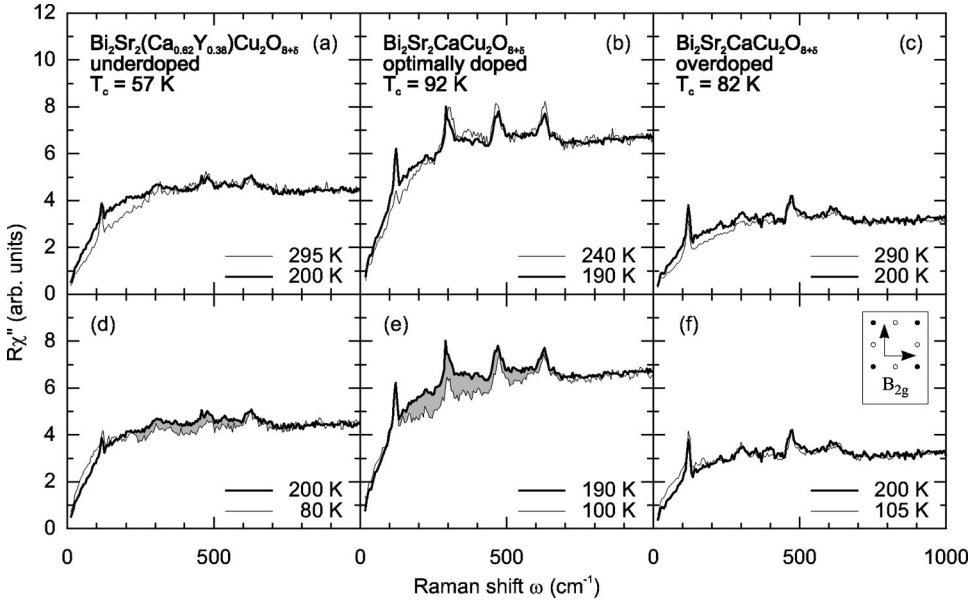


FIG. 6. $B_{2g}$ spectra for Bi2212 at different doping levels as indicated for $T>T_c$. The shaded areas indicate the anomalous loss of spectral weight.

transfer, $\mathbf{q}=0$. Frequency-independent factors such as the density of states at the Fermi energy and units are included in $R_{\gamma\gamma}$. For simplicity we will drop the momentum dependence and the polarization (vertex) indices $\gamma$ and use a dimensionless version of the response function in the following.

Figure 5 shows the spectral response of Y123 in the normal state after division by the Bose factor according to Eq. (1). For clarity two temperature ranges are plotted separately. Above a characteristic temperature $T^*$[61] the variation of the spectra is conventional [Figs. 5(a)–5(c)] in the sense that no intensity anomalies occur: Spectra with a larger slope $\partial\chi''(\omega)/\partial\omega$ in the limit $\omega\rightarrow 0$ lie above those with smaller slope or, more physically, shorter lifetime $\tau$. For $T<T^*$ spectral weight is lost in the range below 800 $\mathrm{cm}^{-1}$ [Fig. 5(d)–5(f)]. At the same time $\partial\chi''(\omega)/\partial\omega$ continues to increase. Therefore, spectra at low temperatures cross those at $T>T^*$. It seems that for the observability of the effect at higher doping levels the samples have to be very pure and well ordered. The anomaly associated with the pseudogap could actually not be identified unambiguously in samples from earlier generations.[8] In the present samples the anomaly is still very weak beyond optimal doping but can be resolved clearly in the data. Consequently, in the almost perfectly ordered overdoped sample with an oxygen content close to $O_{7.0}$ the pseudogap can be seen better than in the optimally doped one with oxygen vacancies and clusters.[63] In the same way two-magnon scattering is seen only in Y123(7.0). Given the influence of disorder in the various samples the results obtained for Bi2212 (Fig. 6) are in qualitative agreement with those for Y123.

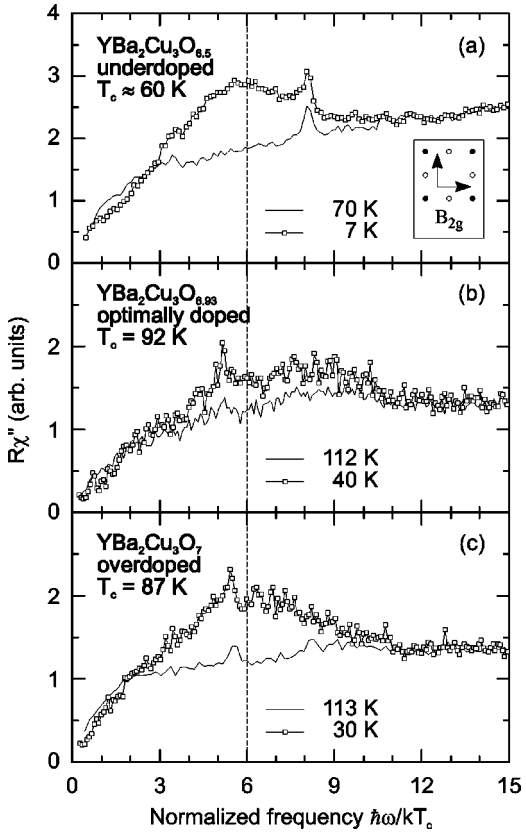


FIG. 7. $B_{2g}$ spectra for superconducting Y123 at different doping levels as indicated.

Spectra for the superconducting state are plotted in Figs. 7 and 8. Here the data are shown as a function of energy units normalized to the respective transition temperatures in order to demonstrate the scaling of the peak maxima with $T_c$. The maxima are at approximately 6 and 7 in units of $k_BT_c$ for Y123 and Bi2212, respectively. The gain in intensity in the range from $3k_BT_c$ to $12k_BT_c$ is generally higher in Y123 although there are differences depending on the doping. According to theoretical considerations[64] this is most likely related to the degree of disorder which certainly varies from sample to sample and which is expected to be higher in Bi2212 with various sources of imperfections. Somewhat unexpectedly but reproducibly,[55,56] no pair-breaking peaks are found at the $A_{1g}$ and $B_{1g}$ symmetries in the underdoped samples (Figs. 9 and 10). Moreover, we hardly find any temperature dependence of the continua at these symmetries in the entire range between 10 and 300 K. However, a couple of phonons gain considerably in intensity upon cooling.[9,65,66]

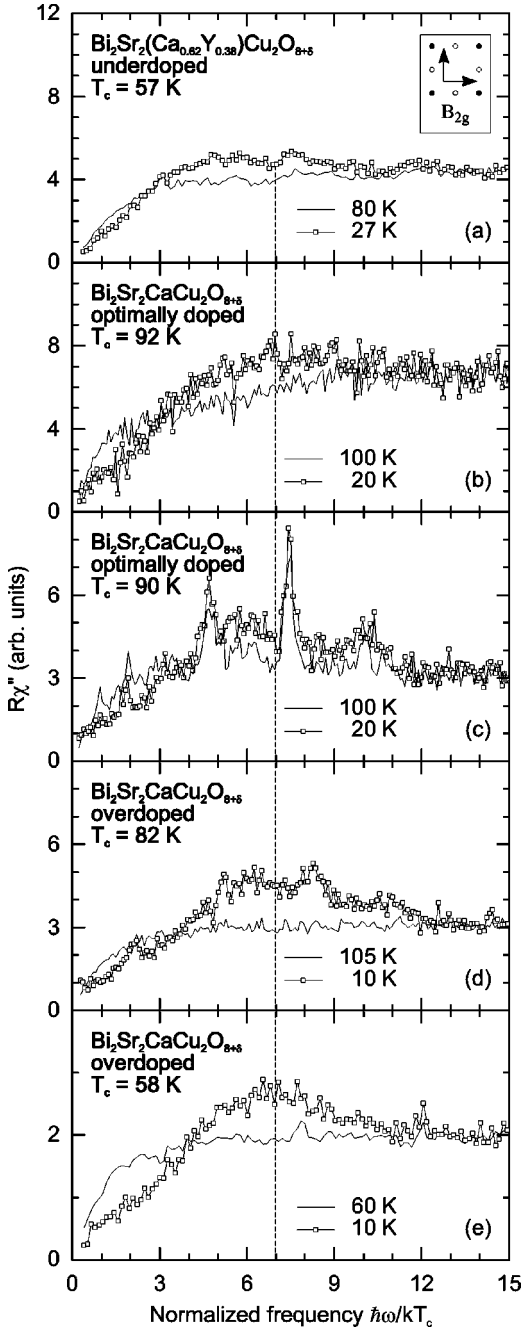


FIG. 8. $B_{2g}$ spectra for superconducting Bi2212 at different doping levels as indicated.

## V. ANALYSIS

The purpose of this section is to analyze the electronic Raman spectra of metallic samples at frequencies up to approximately 1000 $cm^{-1}$ in a more complete way than done previously. As discussed in the preceding section we have good reasons to assume that the cross section in this energy range comes predominantly from carrier fluctuations. Hence we can obtain information about the carrier dynamics. To date only the $\omega=0$ limit has been considered. For the study of the dynamical response we adopt a method which has been introduced by Götze and Wölfle[33] for the current-current correlation function and which has been used subsequently for the analysis of infrared data.[13,32] In this method the relaxation rate $\Gamma=1/\tau$ is replaced by $-iM$ where

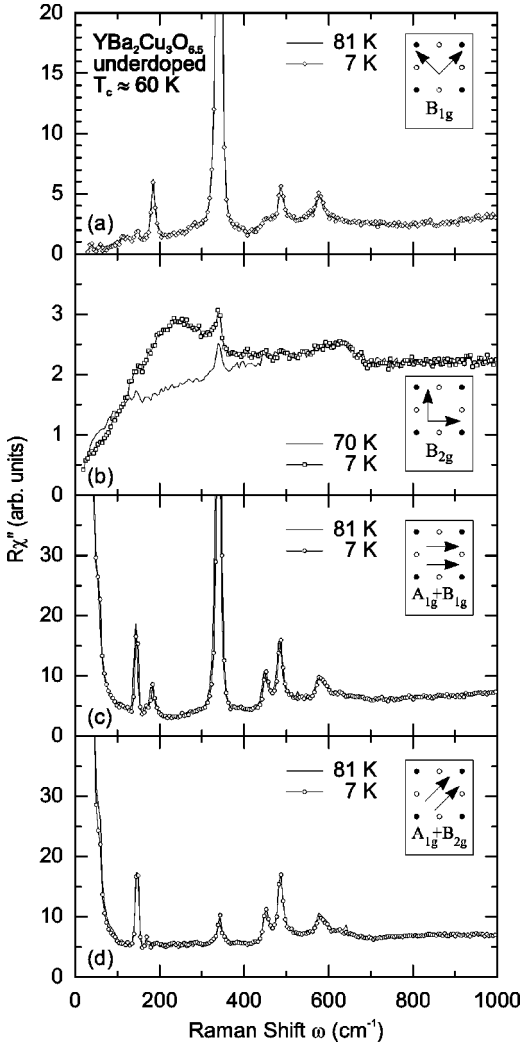


FIG. 9. Raman spectra for underdoped Y123 for $T\simeq T_c$ and $T\ll T_c$ at all main polarizations.

$M(\omega)=\omega\lambda(\omega)+i\Gamma(\omega)$ is the complex memory function. $\Gamma(\omega)$ and $1+\lambda(\omega)$ are the (Raman) relaxation rate and mass-enhancement factor, respectively. The conditions for the applicability are discussed in Ref. 33.

We will give a summary of the relevant expressions here and then analyze the data presented above. A complete description of the formalism can be found in the Appendix.[66,67]

### A. Model

With all vertex indices $\gamma$ dropped the complex Raman response function $\chi(\omega)$ in terms of the memory function $M(\omega)$ is given by[37,66]

$$\chi(\omega)=\frac{M(\omega)}{\omega+M(\omega)}; \tag{2}$$

hence the imaginary part describing the spectra [see Eq. (1)] reads

$$\chi''(\omega)=\frac{\omega\Gamma(\omega)}{\{\omega[1+\lambda(\omega)]\}^2+[\Gamma(\omega)]^2}. \tag{3}$$

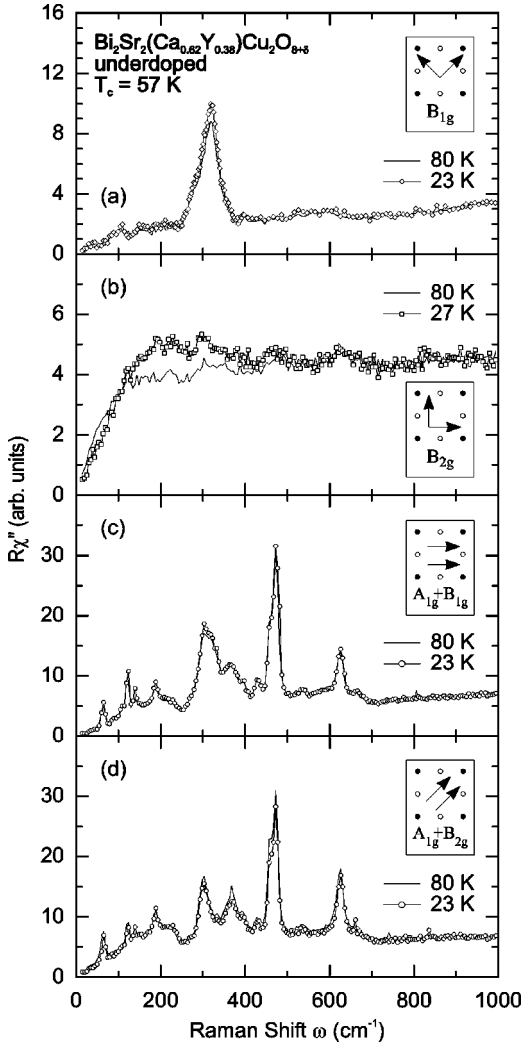


FIG. 10. Raman spectra for underdoped Bi2212 for $T \simeq T_c$ and $T \ll T_c$ at all main polarizations.

We define the function $I(\omega,T)$ which is related to the measured Raman spectra $\dot{N}(\omega,T)$ by

$$I(\omega,T)=\frac{\dot{N}(\omega,T)}{\omega\{1+n_B(\omega,T)\}}, \tag{4}$$

and obtain expressions for the Raman relaxation rate $\Gamma(\omega)$ and the mass-enhancement factor $1+\lambda(\omega)$,

$$\Gamma(\omega)=R\frac{I(\omega)}{[I(\omega)]^2+[\omega K(\omega)]^2}, \tag{5}$$

$$1+\lambda(\omega)=R\frac{K(\omega)}{[I(\omega)]^2+[\omega K(\omega)]^2}. \tag{6}$$

$\omega K(\omega,T)$ is the Kramers-Krönig (KK) transform of $I(\omega,T)$; hence

$$K(\omega)=-\frac{2}{\pi}\wp\int_0^{\omega_c} d\xi\frac{I(\xi)}{\xi^2-\omega^2}, \tag{7}$$

and the normalizing factor $R$ is fixed by a sum rule,

$$R=\frac{2}{\pi}\int_0^{\omega_c} d\omega I(\omega). \tag{8}$$

Since in our case $I(\omega)$ approaches a constant in the dc limit and decays approximately as $1/\omega$ at high frequencies, the integral for $K(\omega,T)$ [Eq. (7)] converges fast as long as the upper cutoff frequency $\omega_c$ is larger than $\omega$ (a factor of 3–5 is satisfactory according to our tests). $R$ depends on $\omega_c$ only logarithmically. For the study of carrier properties a typical value for $\omega_c$ is the bandwidth, here $1\ \text{eV}<\hbar\omega_c<2\ \text{eV}$. $\Gamma$ has the same unit as $\omega$.

Several remarks seem appropriate.

(i) The choice of $\omega_c$ can be cross-checked by looking at the frequency dependence of $1+\lambda(\omega)$. The mass enhancement should asymptotically approach 1 at large energies; in particular it cannot be smaller than unity in a system of nonlocalized carriers. The strongest influence on $1+\lambda(\omega)$ originates from the constant $R$ which, in turn, is the only quantity with a measurable dependence on $\omega_c$. So there exists a second constraint for $R$.

(ii) If the spectral dependence of $\Gamma(\omega)$ and $1+\lambda(\omega)$ resulting from the analysis cannot be described by sufficiently smooth functions, the physical meaning of the analysis is questionable.[33] There are no restrictions as to the high-energy behavior of $\Gamma(\omega)$ and $1+\lambda(\omega)$. The only requirement is a sufficiently rapid convergence of the integrals (7) and (8).

(iii) Due to the vertices, the Raman memory function can be quite different from the one for the conductivity as introduced by Götze and Wölfle.[33] The respective corrections are discussed in the literature.[31] It should be noted that the vertices themselves can well have different frequency dependences.

(iv) The analogy between Raman and conductivity does not exist any more below $T_c$ since the superconducting coherence factors[68] are densitylike and currentlike, respectively. Nevertheless, the carrier lifetime can still be derived from the optical conductivity[7] and from the Raman spectra[37,69] in a two-fluid approximation. As compared to IR the analysis is more complicated for Raman and has not been attempted yet.

(v) The complex conductivity $\sigma(\omega)=\sigma'(\omega)+i\sigma''(\omega)$ can be expressed in terms of $M(\omega)$,[33]

$$\sigma(\omega)=i\varepsilon_0\omega_{pl}^2\frac{1}{\omega+M(\omega)}, \tag{9}$$

with

$$\omega_{pl}^2=\frac{ne^2}{\varepsilon_0 m}. \tag{10}$$

Here $e$ and $m$ are the electronic charge and mass, respectively. $n$ is the density of carriers and $\varepsilon_0$ is the permittivity of vacuum. It is well known that a sum rule can be obtained for the real part of the conductivity (see also the Appendix),

$$\frac{2m}{\pi e^2}\int_0^{\infty}\sigma'(\omega)d\omega=n. \tag{11}$$

The conductivity sum rule, Eq. (11), holds strictly, in particular, at the transition to the superconducting state where

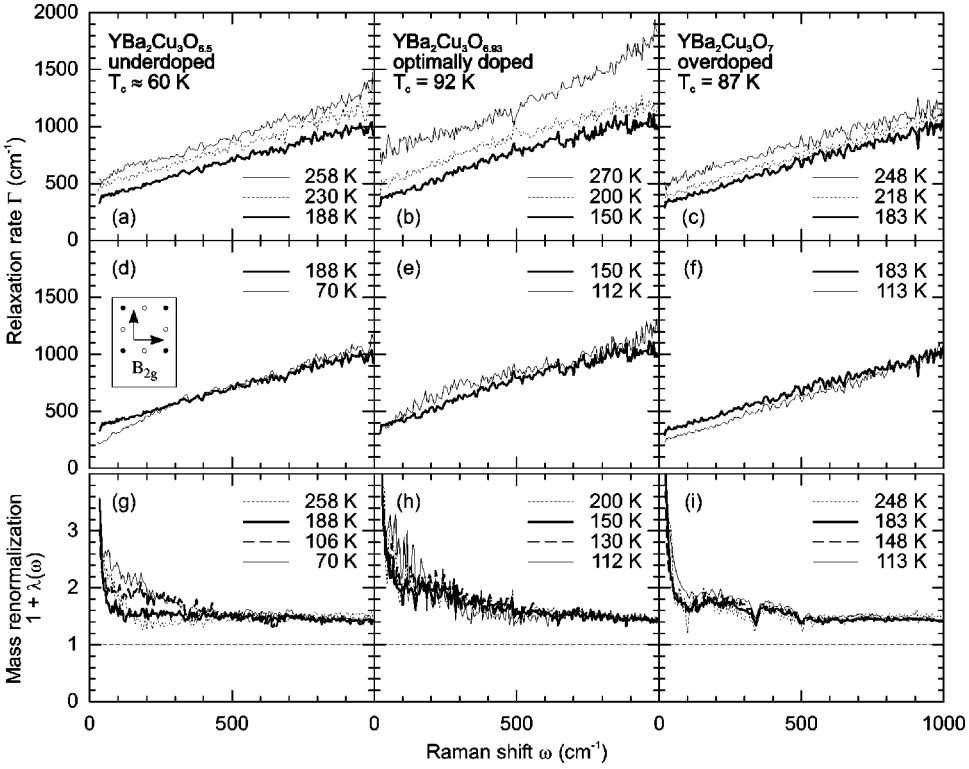


FIG. 11. Dynamical relaxation rates $\hbar\Gamma(\omega,T)=\hbar/\tau$ (a)–(f) and mass renormalization factors $1+\lambda(\omega,T)$ (g)–(i) for Y123 as derived from the $B_{2g}$ spectra via Eqs. (5) and (6). For all temperatures the samples are not superconducting.

the number of Cooper pairs can be determined from the loss of spectral weight at finite frequencies. At first glance, sum rule (8) indicates the existence of a similar conservation law for the Raman response. However, $R$ in contrast to the number of carriers $n$ is not a conserved quantity, because the Raman response function derives from the generalized density-density correlation function[60] which, as opposed to the usual density operator, does not commute with the interaction part of the Hamiltonian. In the superconducting state a completely new scattering channel opens up and $R$ can increase considerably. In the normal state, too, there is no reason for $R$ to be, for instance, temperature independent. However, $R$ does not change significantly for $T_c<T<330$ K. In the limit $\omega\rightarrow 0$ the Drude expression for the dc resistivity $\rho_0(T)$ is recovered from Eq. (9),

$$\rho_0(T)=\frac{\Gamma_0(T)}{\varepsilon_0\omega_{pl}^2}, \tag{12}$$

where $\Gamma_0(T)$ is the scattering rate in the static limit.

### B. Application to the Raman data

We calculate now dynamical scattering rates and mass-enhancement factors using the procedure described in the previous section. First, however, the phonons have to be subtracted out. This is a straightforward procedure in most of the cases as they depend only weakly on temperature. Only the $B_{1g}$ phonon at 340 $\mathrm{cm}^{-1}$ in Y123 requires an individual treatment, and additional noise resulted from that manipulation occasionally. In $B_{2g}$ symmetry, which we are predominantly interested in, the contributions from vibrational modes to the spectra are generally small and can be dealt with easily.

In Fig. 11 we plot dynamical relaxation rates and mass-enhancement factors for differently doped metallic samples of Y123 which have been determined from the spectra using Eqs. (5) and (6). For the KK transformation to be performed the response below 15–30 $\mathrm{cm}^{-1}$ is linearly extrapolated to zero as inevitably required by the antisymmetry of $\chi''(\omega)$. The spectra beyond 1500 $\mathrm{cm}^{-1}$ were extrapolated by a constant since the observed increase does apparently not come from carrier excitations (see Fig. 4 and Sec. VI), the cutoff frequency was set at $\hbar\omega_c=10\,000$ $\mathrm{cm}^{-1}$. The influence of the extrapolation and of the cutoff on the magnitudes of $\Gamma$ and $1+\lambda$ is of the order of 10%. The spectral shape at $\hbar\omega \leqslant 1000$ $\mathrm{cm}^{-1}$ is not resolvably affected for $\hbar\omega_c \geqslant 3000$ $\mathrm{cm}^{-1}$.

For clarity, the temperature ranges above and below $T^*$ are plotted separately. $\Gamma(\omega,T)$ has little structure and is essentially increasing linearly with frequency. For $T>T^*$ the relaxation rates $\Gamma(\omega,T)$ differ only by a constant offset, which is approximately proportional to the temperature, and can be well represented by

$$\Gamma(\omega,T)=\alpha\omega+\Gamma_0(T), \tag{13}$$

where $\alpha$ is a constant varying between 0.4 and 1.5 for the samples studied. $\Gamma_0(T)$ is the static scattering rate, and at optimal doping one finds $\hbar\Gamma_0(T)=\beta k_B T$. $\beta$ is of order 2, in satisfactory agreement with ordinary transport and earlier Raman results.[23] For underdoped samples the static relaxation rate does not extrapolate to zero for zero temperature and $\Gamma_0(T\rightarrow 0)>0$. If the temperature is reduced below $T^*$, $\Gamma(\omega,T)$ starts to develop a kink at approximately 400 $\mathrm{cm}^{-1}$ which is more pronounced for the underdoped sample [Fig. 11(d)] but also clearly visible at higher doping. The relaxation rate for $\omega\rightarrow 0$, $\Gamma_0$, continues to decrease in a similar way as above $T^*$, i.e., linear in temperature. For $\omega$

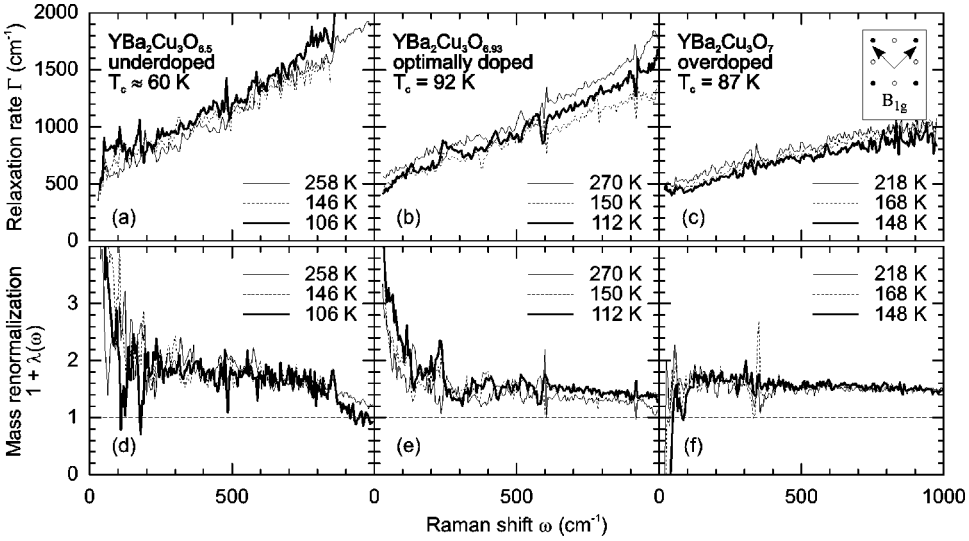


FIG. 12. Dynamical relaxation rates $\hbar\Gamma(\omega,T)=\hbar/\tau$ (a)–(c) and mass renormalization factors $1+\lambda(\omega,T)$ (d)–(f) for Y123 as derived from the $B_{1g}$ spectra via Eqs. (5) and (6) at $T>T_c$.

$>500$ cm$^{-1}$ the temperature dependence becomes much weaker.

The mass enhancement $1+\lambda(\omega,T)$ has little dependence on temperature above $T^*$ and has structure only at low energies while approaching a value between 1 and 2 above 500 cm$^{-1}$ [Figs. 11(g)–11(i)]. This demonstrates that the approach and, in particular, the normalization through the sum rule, Eq. (8), return qualitatively correct results in the far IR range as interactions can only enhance the band mass, implying $\lambda(\omega)\geqslant 0$. The behavior for $\hbar\omega\leqslant 20$ cm$^{-1}$ is not quite clear since the quality of the data is reduced close to the laser line. It appears that there is a weak (logarithmic) divergence at $\omega=0$. Since $\omega\lambda$ and $\Gamma$ are KK related, this is a direct consequence of the linearity of $\Gamma(\omega)$ down to $\omega=0$. Indeed, $\lambda(\omega=0)$ is finite only if $\Gamma(\omega\rightarrow 0)$ is ''rounded off'' or more precisely if $\partial\Gamma(\omega\rightarrow 0)/\partial\omega=0$. This, however, cannot be decided on the basis of the existing data. For $T_c<T<T^*$ a substantial increase of $1+\lambda(\omega,T)$ is found in the low-energy range.

The results for the $B_{1g}$ symmetry are shown in Fig. 12. In contrast to the $B_{2g}$ symmetry not only the zero-frequency extrapolation value and its temperature dependence but also the frequency dependence changes. If we assume that $\Gamma(\omega)$ still varies approximately linearly with frequency according to Eq. (13), the parameter $\alpha$ changes from 1.4 in the underdoped sample to 1 and 1.5 in the optimally doped and the overdoped one, respectively. In addition to that $\Gamma(\omega)$ shows the tendency to saturate for $\hbar\omega>500$ cm$^{-1}$ in the overdoped sample [Fig. 12(c)] while still increasing linearly in the underdoped and the optimally doped samples [Figs. 12(a) and 12(b)]. In the dc limit the relaxation rates $\Gamma_0(T)$ decrease with $T$ in the overdoped and in the optimally doped

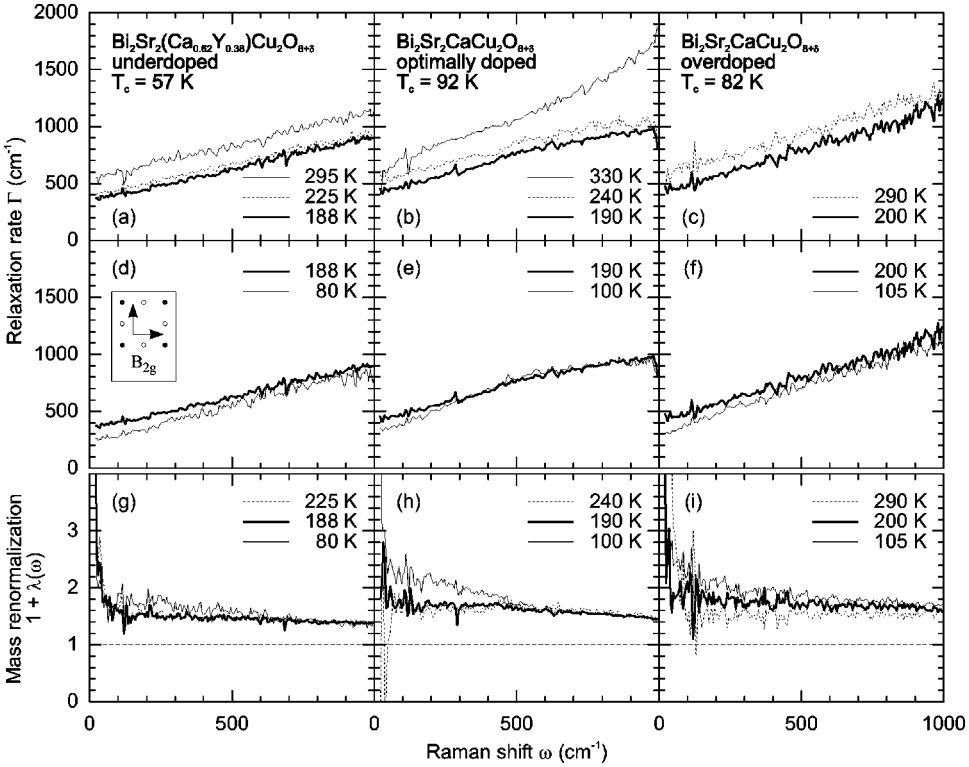


FIG. 13. Dynamical relaxation rates $\hbar\Gamma(\omega,T)=\hbar/\tau$ (a)–(f) and mass renormalization factors $1+\lambda(\omega,T)$ (g)–(i) for Bi2212 as derived from the $B_{2g}$ spectra via Eqs. (5) and (6) (see text) at $T>T_c$.

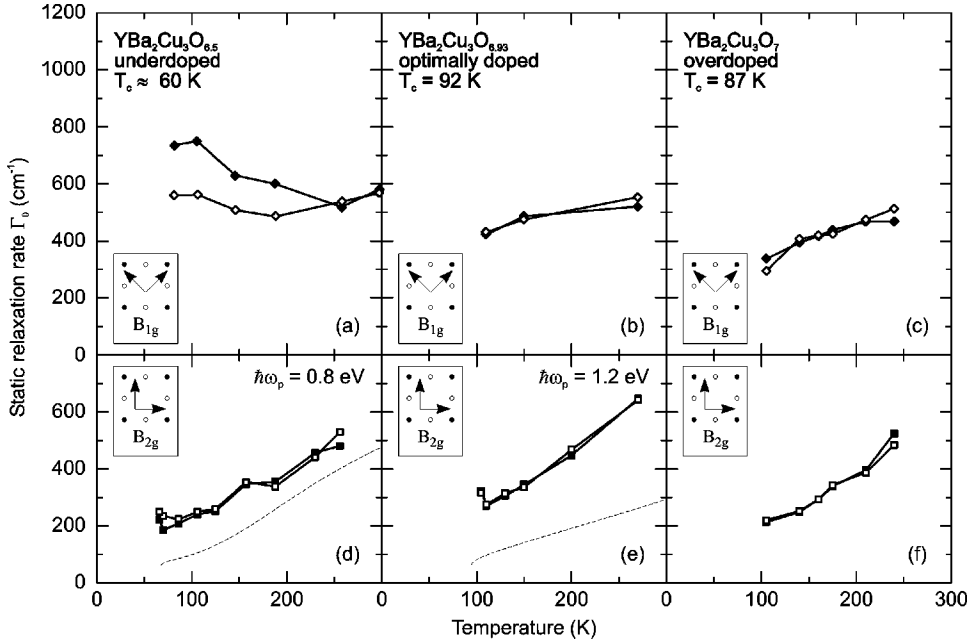


FIG. 14. Static (dc) relaxation rates $\hbar\Gamma_0(T)$ for Y123 for $B_{1g}$ (a)–(c) and $B_{2g}$ (d)–(f) symmetry at $T>T_c$. The error bars are approximately 10%. Open symbols represent the data derived via Eq. (14); solid symbols show the zero-frequency extrapolation values of the dynamical relaxation rates plotted in Fig. 11. The data are scaled to each other. Typical differences are of the order of 30% or less. The dashed lines in (d) and (e) are relaxation rates calculated from the resistivity of comparable samples through Eq. (12) (Ref. 71). The (renormalized) plasma frequencies are taken from Ref. 49.

samples. In the underdoped one $\Gamma(\omega,T)$ generally increases with decreasing $T$, and the overall magnitude is larger by more than a factor of 2. In optimally doped Y123 in both $B_{2g}$ and $B_{1g}$ symmetries the relaxation rates at 112 K deviate slightly from the general trend [Figs. 11(e) and 12(b), respectively] as does $\Gamma_0$ later on [see Fig. 14(e) below]. Most likely this is an artifact due to surface contamination. As an effect of the phonon-subtraction procedure and of the influence of the laser line the results for the mass enhancement become noisy, in particular at small energies. Above some 200 $cm^{-1}$ they are qualitatively similar to those at $B_{2g}$ symmetry at low and optimal doping [Figs. 12(d) and 12(e)]. In the overdoped sample $\lambda$ seems to be close to zero in the whole frequency range [Fig. 12(f)]. Neither for $\Gamma(\omega,T)$ nor for $1+\lambda(\omega,T)$ characteristic changes can be found around $T^*$.

The $B_{2g}$ results for differently doped Bi2212 samples are compiled in Fig. 13. They exhibit qualitatively similar features as those in Y123. Generally, the structures related to the pseudogap are weaker and found at somewhat higher energies at approximately 600 $cm^{-1}$. On account of the larger number of phonons in Bi2212 the data for $1+\lambda(\omega,T)$ are less stable than in Y123 [see Figs. 13(g)–13(i)], and the qualitative change in the pseudogap state is not seen as clearly as in underdoped Y123 [cf. Figs. 11(g) and 13(g)]. We suspect that the presence of structures related

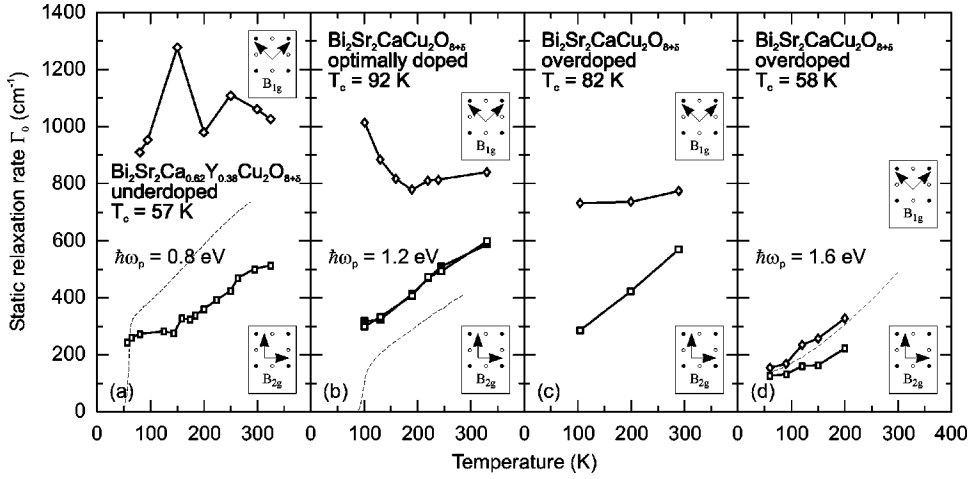


FIG. 15. Static relaxation rates $\hbar\Gamma_0(T)$ for Bi2212 for $B_{1g}$ and $B_{2g}$ symmetry at $T>T_c$ using the same symbols as in the previous figure. The error bars are approximately $\pm 10\%$. The dashed lines in (a), (b), and (d) are relaxation rates calculated from the resistivity through Eq. (12). In (a) and (b) the resistivities $\rho(T)$ have been measured for the respective samples; in (d), $\rho(T)$ is taken from Ref. 72 as are all plasma frequencies.

to the pseudogap can be suppressed by imperfections in the sample, and it is very likely that Y doping of Bi2212 affects the $CuO_2$ planes stronger than oxygen deficiencies in Y123. In the superconducting state we will observe consistently the pair-breaking structures to be less pronounced in Y-doped Bi2212.

## VI. DISCUSSION

The physical quantities which can be obtained on the basis of the proposed model allow additional insights into properties of the cuprates. We will first focus on the static (dc) limit and discuss the relationship to other experiments. Later on, we will try to arrive at a better understanding of the pseudogap and the superconducting gap and their respective evolution with doping and temperature.

### A. Static limit

Static relaxation rates have already been derived from the Raman data.[23,39,55,70] In order to obtain absolute numbers model assumptions as to the spectral shape of the response were used such as a relaxation rate $\Gamma(\omega,T)=\sqrt{[\alpha\omega]^2+[\Gamma_0(T)]^2}$ where $\Gamma_0(T)=\Gamma(\omega=0,T)$.[39,70] The frequency dependence was limited to $\Gamma$ while $\lambda$ was set identical zero (see, e.g., Refs. 39 and 70). This is a reasonable guess as we find here $1+\lambda(\omega)$ to be constant and close to unity for a fairly large frequency range (see Figs. 11 and 13). In addition, the influence of $\lambda$ is very small in the limit $\omega=0$ [see Eq. (3)]. It is important to note, however, that this form of $\Gamma(\omega,T)$ returns realistic results only in the limit $\omega=0$ while failing for $\omega\neq 0$. For finite $\omega$ the correct frequency dependence is rather described by Eq. (13) which, in turn, does not at all allow one to fit the data with $\lambda\equiv 0$. This detail shows that the proper treatment leads to qualitatively different results.

A reasonable estimate for $\Gamma_0(T)$ independent of the details of the spectral shape of $\chi''(\omega)$ can be obtained directly from an extrapolation of the scattering intensity to $\omega=0$, $\dot{N}(\omega\rightarrow 0,T)$, which is proportional to $\tau_0(T)=[\Gamma_0(T)]^{-1}$ in the same way as $\partial\chi''(\omega,T)/\partial\omega$ (see Ref. 38). If $\Gamma(\omega)\propto\omega$ at large energies [see Eq. (13)], the missing constant of proportionality is given by the extrapolation value of $\chi''(\omega\rightarrow\infty)$, in any other case, including constant $\Gamma$, by the maximal value of $\chi''(\omega)$. All these numbers are close to 1/2 at the appropriate frequency $\omega_{1/2}$. Then, for $\hbar\omega_{1/2}\gg k_BT$, we have a rough estimate of the constant, according to Eq. (1) $R=2\dot{N}(\omega_{1/2})$, and the zero-frequency extrapolation value of the relaxation rate $\Gamma_0$ is given by

$$\hbar\Gamma_0(T)=k_BT\frac{2\dot{N}(\omega_{1/2})}{\dot{N}(\omega\rightarrow 0,T)}. \tag{14}$$

For the determination of $R$ we always took the average intensity between 800 and 1000 $cm^{-1}$, $\dot{N}_{1000}$, which was temperature independent in all experiments (see Fig. 1). These arguments rest on quite general principles such as the antisymmetry of the response function and illustrate that the low-energy part of the Raman spectra follows rules which, even if qualitative, provide an idea of the trends and lead already to useful conclusions independent of the origin of the intensity: Whenever the response is collision limited, i.e., $\mathbf{v}_F\cdot\mathbf{q}\ll\Gamma$ with $\mathbf{v}_F$ the Fermi velocity and $\mathbf{q}$ the momentum transfer, the slope of the low-energy part of the spectra scales with the lifetime of the respective excitation.

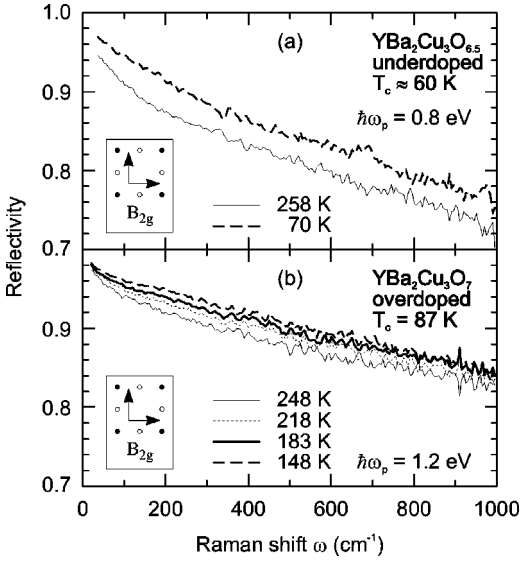


FIG. 16. Reflectivities as derived from the $B_{2g}$ dynamical scattering rates $\Gamma(\omega,T)$ and mass renormalization factors $1+\lambda(\omega,T)$ for overdoped and underdoped Y123 at various temperatures as indicated. The (renormalized) plasma frequencies are taken from Ref. 49.

The results for the static limit are consistent with those obtained in the previous section. The temperature dependence is reproduced almost identically. For the magnitude discrepancies of 10% or 20% are typical. Figures 14 and 15 show the results for $\hbar\Gamma_0(T)$ as obtained for Y123 and Bi2212, respectively, from both the extrapolation of the intensity according to Eq. (14) and the extrapolation of the dynamical scattering rate $\Gamma(\omega,T)$ to $\omega=0$ as shown in Figs. 11 and 13. The magnitudes have been adjusted to facilitate the comparison. The agreement with the old data[70] is of similar quality, and we have to conclude that the relaxational behavior in the dc limit is a stable result. The most striking fact is the difference between the $B_{1g}$ and $B_{2g}$ symmetries being qualitatively similar in the two compounds: Towards low doping the $B_{1g}$ scattering rates increase, and their variation with temperature $\partial\Gamma_0(T)/\partial T$ change sign from positive to negative.

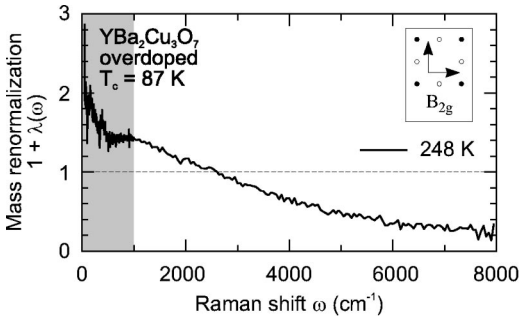


FIG. 17. Mass renormalization $1+\lambda(\omega)$ as calculated from the $B_{2g}$ Raman response of overdoped Y123 in an extended energy range. Similar results are obtained for other doping levels.

### B. Other experiments

The properties of the carriers have been investigated by several other methods such as ordinary, Hall, and heat transport, optical (IR) conductivity, electron tunneling, and ARPES. Most of these experiments are indicative of a strong momentum dependence of the relaxation time $\tau_{\mathbf{k}}(\omega,T)$ without, however, converging into a unified picture.

As demonstrated in Figs. 14 and 15 the scattering rates found here at $B_{2g}$ symmetry in the limit $\omega=0$ show a similar evolution with temperature and doping as ordinary transport. For comparison we plotted dc scattering rates as obtained from the resistivities through the Drude formula, Eq. (12), represented as energies $\hbar\Gamma_0$. For Y123 all resistivities and for the Bi2212 part of the resistivities are taken from the literature[71,72] as are the plasma frequencies in general.[49,72] Throughout the paper renormalized plasma energies are used. For Y123 *a*-axis data have been selected as the $B_{2g}$ Raman data are insensitive to chain contributions. The discrepancies between Raman and transport data are smaller than some 30%, and the qualitative change with doping $p$, e.g., the zero-temperature extrapolation values $\Gamma_0(p,T\rightarrow 0)$ and the slopes $\partial\Gamma_0(p,T)/\partial T$, of the relaxation rates are well reproduced. Independently, very good agreement was found between ordinary and optical transport.[6,7,73] Up to this point we apparently wind up with a consistent picture, and the $B_{2g}$ Raman response probes the relaxational behavior in the zero-frequency limit as does IR and transport.

At finite energies, the $B_{2g}$ Raman results and the IR data for $\Gamma(\omega)$ agree also rather well up to energies of approximately 1500 $\mathrm{cm}^{-1}$.[6,7,73] As in IR spectroscopy the magnitude of the scattering rates does not vary significantly with doping, implying that the variation of the dc resistivity with doping is apparently not simply an effect of a change in the lifetime. It is rather a combination in that the zero-temperature offset is due to the lifetime while the increase of the slope originates from the change of the plasma frequency [see Eq. (12) and Ref. 49]. The differences between the IR and Raman results are more pronounced for $1+\lambda(\omega,T)$. The qualitative change with temperature and the order of magnitude are still similar (see, e.g., Ref. 32); however, the range in which the effective mass depends on energy is confined to some 500 $\mathrm{cm}^{-1}$ in our experiment while being very wide in IR.[73]

ERS and IR data can be directly compared when the dynamic reflectivity is calculated from the light-scattering results for $\Gamma$ and $\lambda$ via the standard formula. In Fig. 16 we show the results for underdoped and slightly overdoped Y123 using typical (renormalized) in-plane plasma frequencies $\omega_{pl}^{a}$ obtained from the reflectivity with light polarized along the *a* axis. As the contribution of the chains is suppressed the reflectivity is smaller than for random polarization but both the temperature and the frequency dependences are well reproduced, in particular for the overdoped sample. For the underdoped one the influence of the pseudogap below $T^*\simeq 200$ K manifesting itself as a kink in the IR reflectivity between 500 and 800 $\mathrm{cm}^{-1}$ cannot be resolved in the ''Raman reflectivity'' while being very pronounced in the far IR.[74] This difference is remarkable as the relaxation rates obtained from Raman and IR scattering are quite similar. Apparently, the discrepancies in the ''reflectivities'' are related to the more pronounced differences in the respective mass renormalizations which are not understood at the moment. As already pointed out the present analysis neglects all details of the interaction between photons and electrons (vertex corrections), and one should probably start here for a better understanding. Nevertheless the similarities of the properties found by ordinary and optical transport and $B_{2g}$ Raman scattering prevail in the range $\hbar\omega<1500$ $\mathrm{cm}^{-1}$.

At high energies ($\hbar\omega>1500$ $\mathrm{cm}^{-1}$) Raman scattering and IR results cannot be compared anymore which is most strikingly demonstrated in a plot of the mass renormalization. $1+\lambda(\omega)$ as derived from Raman scattering drops significantly below unity for $\hbar\omega>2500$ $\mathrm{cm}^{-1}$ after a plateau extending over 500–1000 $\mathrm{cm}^{-1}$ (Fig. 17). This is a clear indication that the cross section cannot come from carriers only as already suspected earlier (see Fig. 4) since negative $\lambda$'s are unphysical in a metallic system. It should be emphasized that the magnitude of $1+\lambda$ is determined independently by the sum rule, Eq. (8), in the same way as the relaxation rate $\Gamma$ which, in turn, is found to be consistent with other experiments. Consequently, an absolutely nontrivial result is shown in Fig. 17. We arrive at the conclusion that there is a lot of evidence for Raman scattering at $B_{2g}$ symmetry to probe carrier excitations in a range up to 1500 $\mathrm{cm}^{-1}$. Beyond this range additional channels contribute to the inelastic cross section which essentially do not vary with doping.

We wish to point out again that IR spectroscopy and Raman scattering cannot be expected to return identical results even if the same type of excitation is probed. First, different parts of the Fermi surface are projected out by the two methods. In a tetragonal system, for instance, the conductivity is completely isotropic in the basal plane. Apparently, however, the $B_{2g}$ Raman response, at least at small frequencies, and ordinary and optical conductivity emphasize similar parts in momentum space, i.e., those along the diagonals.

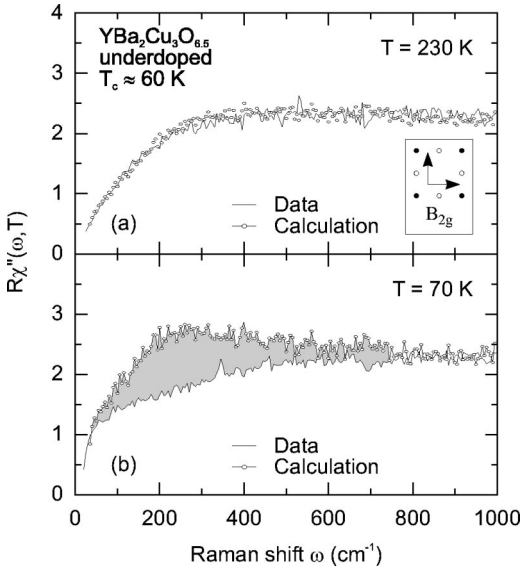


FIG. 18. Extrapolated ''normal'' spectra for the pseudogap state, $T<T^*$. As demonstrated in (a) the extrapolation procedure works quite well above $T^*$ where the actually measured spectra can be reproduced satisfactorily. In the pseudogap state (b) the deviation from the expected ''normal'' behavior is very pronounced.

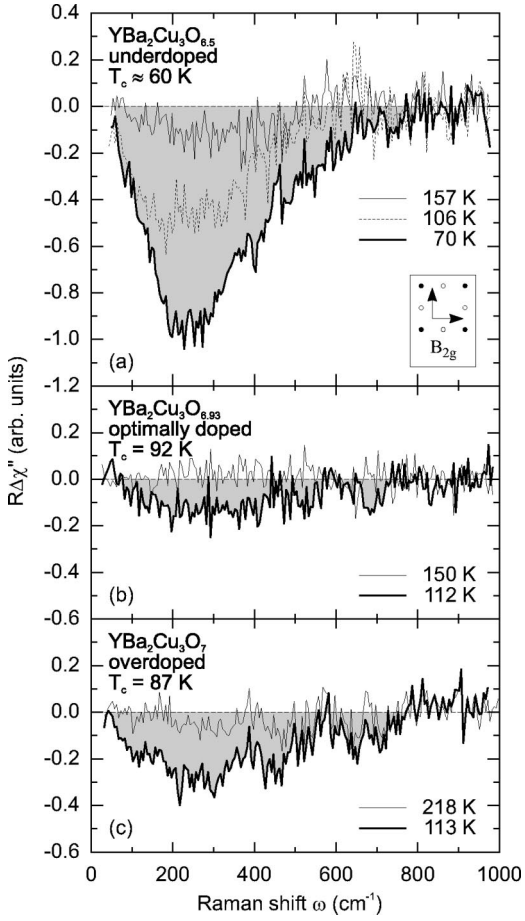


FIG. 19. The pseudogap as a function of temperature and doping for Y123. Shown in the figure is the difference between the experimental and the extrapolated response function $R\Delta\chi''(\omega,T,p)$.

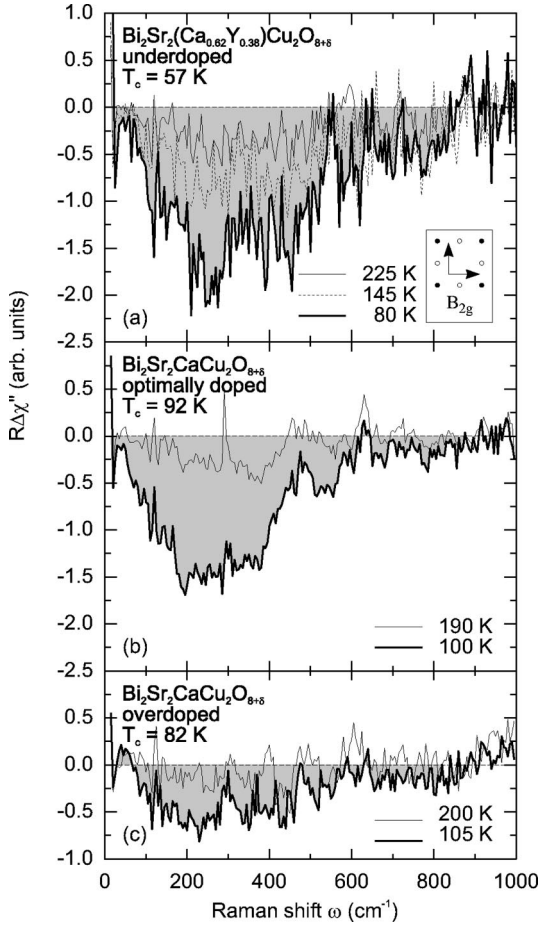


FIG. 20. The pseudogap as a function of temperature and doping for Bi2212. Shown in the figure is the difference between the experimental and the extrapolated response function $R\Delta\chi''(\omega,T,p)$.

Second, the bare response functions are renormalized in very different ways (vertex corrections) which depend on the probing energies. The exploration of the latter subject is just at the beginning.

It is obvious that the $B_{1g}$ data cannot be linked to ordinary transport. If there exists a relationship to other transport results at all the dc limits of the ERS data are reminiscent of the Hall resistivity $\rho_{xy}(T,p)$,[75–77] the transverse heat transport[78] (Righi-Leduc effect) or *c*-axis transport.[79] It has indeed been argued that the characteristics of longitudinal and transversal transport are being determined by carriers with momenta along the diagonals and the principal axes, respectively.[76,77] Alternatively, spin-charge separation can lead to different relaxation times.[80] Then the $B_{1g}$ rate would correspond to the spin degrees of freedom. Indeed, the $B_{1g}$ channel samples magnetic excitations[81] becoming more and more dominant at low doping. Consistently, in strongly overdoped Bi2212 with essentially no magnetic correlations present the scattering rates are almost identical in the two channels (see Fig. 15) while the *a*-*c* anisotropy is still very large.[79] So there are probably two sources for the anisotropy between the $B_{1g}$ and $B_{2g}$ channels in the Raman data, one reflecting the in-plane anisotropy of electronic properties, the other one being related to the *a*-*c* anisotropy. The in-plane component can be compared to ARPES results. There, the scattering rates derived for momenta close to $(\pi,0)$ increase strongly towards low carrier concentration.[82] In conventional theory only electronic states lead to ARPES spectra like that, and Raman scattering would then just reflect the same strong in-plane anisotropy of carrier properties. It has been shown recently that a strong interaction between electrons and spin fluctuations or scattering of electrons on extended impurities can lead to such properties.[25] It is not clear at the moment how the anisotropy found by Raman scattering can be related to the formation of stripes and the crossover from two-dimensional (2D) to 1D behavior in the pseudogap phase as proposed by Moshchalkov *et al.*[83] If one applies the same argument as for the chains in Y123, the $B_{2g}$ in contrast to the $B_{1g}$ response would not be expected to be sensitive to properties of stripes running along the Cu-O bonds. In this scenario the similarity between $B_{2g}$ Raman scattering, IR spectroscopy, and transport can only be explained if the overlap between the stripes is substantial and not strictly perpendicular to the bond direction.

We can summarize this section by stating that ordinary and optical transport and $B_{2g}$ Raman scattering at energies below 1000 $cm^{-1}$ can be described consistently in a simple Drude-like picture as long as we limit ourselves to temperatures above $T^*$. At low temperature, $T<T^*$, and low doping, $p\leqslant 0.1$, the scenario turns out to be oversimplified: (i) Qualitatively new behavior is observed in the $B_{2g}$ Raman spectra but the related features are weaker than in IR spectroscopy. (ii) For both Y123 and Bi2212, as well as for LSCO,[8,55,56] no

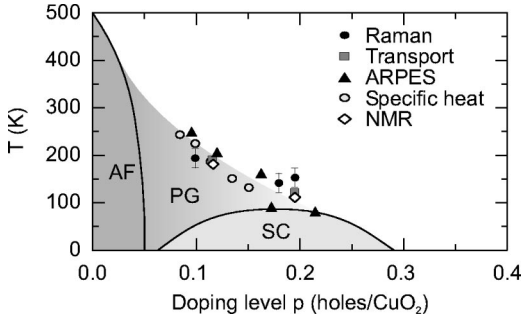


FIG. 21. Comparison of the characteristic temperatures $T^*$ as obtained from different experiments as a function of the number of carriers per $CuO_2$ plane.

signature of the superconducting gap can be observed at $B_{1g}$ symmetry in underdoped samples with $T_c \leqslant 0.7\ T_c^{\max}$. There is no significant change in the spectra either at the pseudogap temperature $T^*$. At present this observation cannot be linked to the ARPES results where the pseudogap is clearly seen for momenta approximately parallel to the principal axes, equivalent to $B_{1g}$ in Raman scattering.

### C. Pseudogap

For underdoped Y123 and Bi2212, $B_{2g}$ results in the pseudogap state have already been described elsewhere.[8,9] Here, we will additionally focus on the doping and temperature dependence and propose a method for the data analysis.

The pseudogap state is characterized by a loss of spectral weight in the frequency range between zero and approximately 800 $cm^{-1}$. This decrease of the scattering cross section is clearly seen in $B_{2g}$ symmetry in underdoped but still superconducting material when the spectra taken at $T_c < T < T^*$ are compared to those at higher temperature. However, it would be more physical to relate ''normal'' and ''pseudogap'' spectra at the same temperature. Since the new state below $T^*$ cannot be suppressed, we try to construct spectra at the respective temperatures. From the temperature dependence at $T > T^*$ we have a fairly good idea of how the ''normal'' evolution of the spectra with temperature should look: The mass enhancement does not change significantly and the scattering rate $\Gamma(\omega,T)$ is essentially linear in frequency in the range of interest. With decreasing temperature a constant offset is subtracted which is approximately proportional to temperature [see Figs. 11 (a)–11(c) and Eq. (13)]. The constant offset is completely determined by the static limit $\Gamma_0(T)$. Therefore, we take $1+\lambda(\omega,T)$ and $\Gamma(\omega,T)$ from above $T^*$, leave $\lambda$ unchanged, shift $\Gamma$ by an appropriate constant in a way that it matches the experimental value of static limit $\Gamma_0(T<T^*)$ at the desired temperature $T$, and plug the quantities into the expression for the normal-state response, Eq. (3). In this way we obtain an estimate of how the normal response $R\chi''(\omega,T)$ should look at temperatures in the pseudogap state. The difference between the extrapolated and the measured spectra $R\Delta\chi''(\omega,T)$ is then a more realistic approximation of the loss in intensity occurring for $T<T^*$. The extrapolation procedure can be checked at high temperatures and is found to be fairly reliable (Fig. 18).

We can now systematically study the dependence of the pseudogap on doping and on temperature. The results, i.e., the reduction of cross section, for Y123 and Bi2212 are plotted in Figs. 19 and 20, respectively. For underdoped material close to $T_c$ the reduction of the response function as a result of the pseudogap has the same order of magnitude as the response itself. The change of the spectra in the new state becomes very small for higher doping levels but can still be observed even if the $T_c$ of the sample is already reduced by more than 10% on the overdoped side (Fig. 20). In Y123 the effect of the pseudogap does not decrease monotonously towards higher carrier concentration and is stronger in the overdoped sample than in the optimally doped one. Since we know from magnetization measurements that the optimally doped sample we used here is less ordered than the overdoped one due to oxygen clustering,[63] it is straightforward to assume that the pseudogap state may escape detection in even slightly disordered material. One of the reasons is the pronounced **k** dependence of the pseudogap as observed by ARPES since scattering from impurities leads always to a mixing of different momenta, hence averaging out effects confined to small parts of the Fermi surface. In a recent ARPES experiment on Bi2212 the effect of disorder due to irradiation with electrons has indeed been studied[84]: With increasing disorder first the gap in the superconducting state is filled in, then the electronic states above $T_c$ are smeared out. In addition, elastic scattering of carriers off defects leads to an independent contribution to the Raman cross section which is not at all affected by the new state. This explains consistently that the effect of the pseudogap (i) is weaker in underdoped Bi2212 with Ca partially replaced by Y, (ii) is reduced in optimally doped Y123 with oxygen clustering, and, simply because of the continuous improvement of the sample quality, (iii) was not observed earlier in Raman scattering. From these considerations, too, we have to conclude

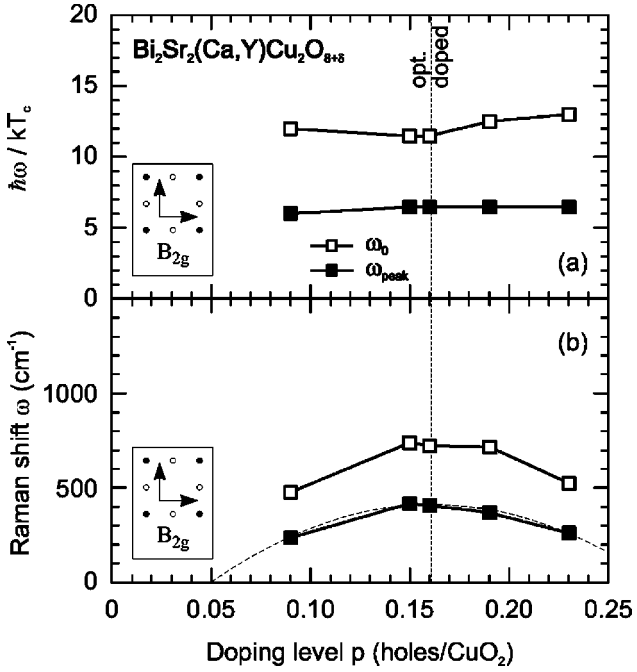


FIG. 22. Peak $\hbar\omega_{\text{peak}}$ and merging $\hbar\omega_0$ frequencies for $B_{2g}$ symmetry in differently doped Bi2212 samples. The dashed line is a parabolic fit to the peak frequencies resembling closely the doping dependence of $T_c$ as described in Ref. 45.

that the Bi2212 sample with $T_c = 92$ K is already on the underdoped side of the phase diagram.

While the maximal amplitude of the spectral change $R\Delta\chi''(\omega_{ps},T,p)$ is doping and temperature dependent both the center of gravity $\hbar\omega_{ps}$ and energy range $E^*$ within which the spectra are subject to changes below $T^*$ are apparently not. We observe them at approximately 200 and at 800 $cm^{-1}$, respectively. $R\Delta\chi''(T,p)$ disappears at a doping-dependent temperature $T^*(p)$. Due to noise and probably also for small instabilities in the measuring conditions, $T^*$ is not very well defined but seems to approach $T_c$ at a not yet clearly determined doping well beyond the optimal one.

The Raman data fit reasonably well to the results found with other methods as long as the characteristic temperature is concerned (Fig. 21). However, it is not yet clear to which extent the results can really be compared. The energy scales are different, and there exists no microscopic model yet which allows a consistent derivation of the various correlation functions. The energy $\Delta_0 \simeq 500$ K (350 $cm^{-1}$) found in ARPES close to $(\pi,0)$ apparently related to the normal-state gap as it is also observed above $T_c$. The difference between $\Delta_0$ and the characteristic energy $E^*$ observed in ERS of approximately a factor of 2, $E^* \simeq 2\Delta_0$ can be understood qualitatively if one recalls that ARPES and ERS are described by single- and two-particle correlation functions, respectively. However, in contrast to Raman scattering where $E^*$ is constant $\Delta_0 \propto T^*$ is observed in ARPES.[85] A similar discrepancy is found in comparison to electron tunneling experiments[10,11] where the energy of the normal-state gap scales with that of the superconducting one. In addition to that, the normal-state gap can even be observed at very high doping levels and temperatures.[11] This has partially inspired an explanation in terms of a charging effect in the insulating layers between the $CuO_2$ planes.[86] On the other hand, in all optical methods similar energy and temperature scales are observed[7,87] although some details are different. The kink in $\Gamma(\omega)$, for instance, is at 400–600 $cm^{-1}$ in Raman scattering while it is at 800 $cm^{-1}$ in IR spectroscopy[7] where we locate $E^*$.

Recently, Naeini and co-workers[56] have studied LSCO by Raman scattering at various doping levels. They found a strong reduction of the $B_{1g}$ cross section at low doping, independent of temperature (see also Refs. 9, 54, and 55) and interpreted it by Fermi surface destruction as proposed, for instance, by Engelbrecht *et al.*[88] or Furukawa *et al.*[89] Since no temperature dependence was found in this study, it is apparent that different subjects are being discussed here and there which nevertheless can be related through a common interaction such as spin fluctuations in a way suggested by Schmalian and collaborators.[90,91]

### D. Superconducting gap and pseudogap

In the current discussion the relationship between the pseudogap and the superconducting gap plays a prominent role (see, e.g., Refs. 13 and 20 and references therein). Since the Raman response is related to a density correlation function, even-parity coherence factors[68] are relevant. They give rise to the occurrence of pair-breaking features in the spectra,[60,92] thus clearly indicating the onset of phase coherence in the superconducting state. Consequently, the existence of a gap or of pairs without phase coherence on the one hand and of coherent pair formation on the other hand leads to fundamentally different structures in the spectra. Hence, Raman scattering can provide qualitatively new information by clearly distinguishing between a normal state and a superconducting gap in a way more similar to Andreev reflection experiments[20] than to ARPES, IR, or electron tunneling.

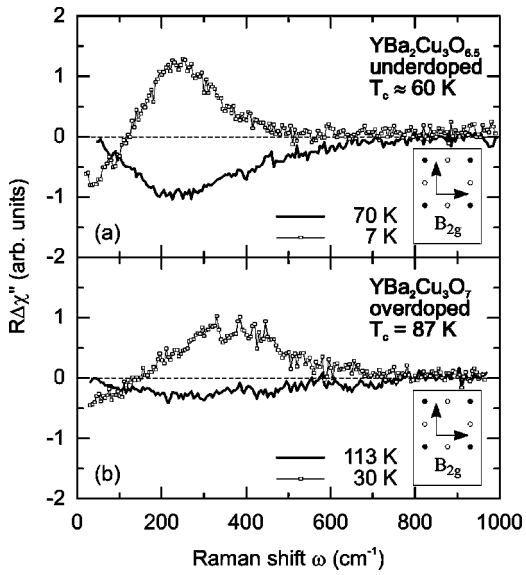


FIG. 23. Pseudogap and superconducting gap at $B_{2g}$ symmetry for two characteristic doping levels in Y123. The results for Bi2212 show the same trend.

The variation with **k** and the symmetry of the SC gap in the cuprates have been discussed exhaustively, and a prevailing $d_{x^2-y^2}$ contribution seems to be widely accepted not only at optimal doping. The spectral dependence of the Raman response is in quantitative agreement with the *d*-wave hypothesis, at least close to optimal doping.[34,36–38,55,93,94] Complications arise both in the overdoped and underdoped ranges of the phase diagram. At high doping levels the spectra seem to be supportive of a reduced anisotropy;[95,96] however, small admixtures of an *s*-wave component can at least qualitatively explain the shift of the peaks.[53] More importantly, the low-frequency power laws clearly show a dominant $d_{x^2-y^2}$ component. For low doping the situation is more complicated as pair-breaking features cannot be found neither at $A_{1g}$ nor at $B_{1g}$ symmetry in samples with a substantially reduced $T_c$ (Figs. 9 and 10).[8,9,23,55,56,97,98] The pair-breaking peaks rather fade away closely below optimal doping.[98] In contrast, superconductivity-induced features can be observed reproducibly in $B_{2g}$ symmetry at all doping levels.[23,55,56,99] For both compounds Y123 and Bi2212, as well as for LSCO,[56] they can be shown to scale with $T_c$ (Figs. 7 and 8). For better visualization normalized and absolute peak frequencies for Bi2212 are plotted in Fig. 22. The peaks are found at approximately $7k_BT_c$. In addition, the response increases linearly over an energy decade (in contrast to the convex shape in the normal state) with the slope $\partial\chi''(\omega,T\simeq 0)/\partial\omega$ scaling with $k_BT_c$ in the same way as the peak frequencies (Fig. 8). The energies $\hbar\omega_0$, where normal and SC spectra merge, exhibit the same scaling behavior as $\hbar\omega_{peak}$, thus demonstrating the spectral shape to be doping independent as well. We conclude, therefore, the gap to be *d*-wave-like at all doping

levels. Consequently, the energy scale relevant for the superconducting state is of the order of $8k_BT_c$ at all doping levels studied.

This is not at all a generally accepted conclusion as many other experiments suggest $\Delta_0$ to scale with $T_c$ at best in the overdoped range and to continuously increase in the underdoped part of the phase diagram where $T_c$ decreases again.[10,102,103] This raises the important question of what is actually measured in the various experiments.[20,104] If low energies, $E \ll \Delta_0$, are considered such as in measurements of the specific heat $c_p$ or of the magnetic penetration depth $\lambda_{ab}$, the gap seems to scale with $T_c$ in the whole doping range while typical high-energy probes, $E \simeq \Delta_0$, such as ARPES find a decoupling of $T_c$ and of what is usually identified with $\Delta_0$. In electron tunneling experiments both types of behavior seem to be observable, in that close to $E=0$ there is scaling[104] while the position of the conductance peaks increases continuously towards low doping.[10,103] It has been argued that the Raman peak frequencies at $B_{1g}$ symmetry also continue to increase in the underdoped range,[95,98] resembling the high values found by tunneling or ARPES.[101] Although most of the recent studies find the Raman peaks to vanish rapidly below optimal doping,[23,55,56,98] the frequency positions and, in particular, the interpretation are still a matter of debate. Part of the problem is related to the strong sample dependence which is almost completely absent in $B_{2g}$ symmetry (cf. Figs. 7 and 8). At $B_{1g}$ symmetry we found differences in the peak frequencies of occasionally 100 $cm^{-1}$ for samples with the same $T_c$ and doping level just as a result of different annealing routes or sample qualities. For this reason we will not pursue the discussion of the $B_{1g}$ response here.

At present, agreement between the different methods can be achieved for small energies. Here, tunneling, penetration depth, and $B_{2g}$ Raman scattering suggest the existence of nodes being characterized by a gap varying as $\Delta(\delta\varphi) = C\delta\varphi$ with $\delta\varphi$ the distance from the node on the diagonal. In addition, the constant $C$ seems to scale with $T_c$. In Andreev reflection experiments $2C$ is found to be close to $6k_BT_c$,[20] in satisfactory agreement with the data presented here. For the limited resolution there are no reliable ARPES data close to the node. Apparently, the $B_{2g}$ Raman data are consistent with the low-energy probes not only in the normal state but also below $T_c$.

In $B_{2g}$ symmetry we can compare the energy scales of the pseudogap and of the superconducting gap directly. In Fig. 23 spectra for two doping levels are shown. In both cases pseudogap data for $T \simeq T_c$ have been replotted from Fig. 19. For the superconducting state we show the difference $R[\chi''(\omega, T \simeq 0) - \chi''(\omega, T_c \rightarrow T \simeq 0)]$ of the data at low temperature and spectra extrapolated from those close to $T_c$ to $T \simeq 0$ using the same procedure as described for the pseudogap (see preceding paragraph). The respective raw data can be found in Fig. 7. In the underdoped sample the difference $R\Delta\chi''$ vanishes for energies larger than $\hbar\omega_0 \simeq 500$ $cm^{-1}$, well below $E^* = 800$ $cm^{-1}$. For Y123(7.0), $\hbar\omega_0$ and $E^*$ coincide. At the same time the superconducting peak moves from 220 to 350 $cm^{-1}$ while the centers of gravity of the pseudogap spectra $\hbar\omega_{ps}$ remain almost unchanged at 200–250 $cm^{-1}$. This may demonstrate that we cannot find a scaling behavior of the two gaps. $E^*$ is apparently an energy scale which is also observed in IR spectroscopy[7] where it seems to be as independent of doping as here. Since $E^*$ is approximately constant, it is tempting to compare it with the magnetic exchange energy $J \simeq 100$ meV being of similar magnitude. There is no energy scale which compares sufficently well with the magnitude of the spin gap [$\Delta_{spin} \simeq 160$ $cm^{-1}$ for underdoped Y123 (Ref. 83)] to motivate an identification. $\hbar\omega_{ps}$ seems to be close in energy but exhibits a different doping dependence.

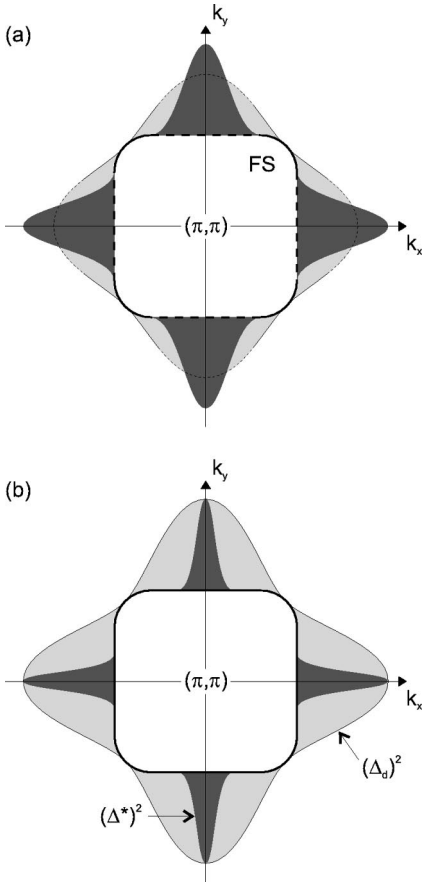


FIG. 24. Variation of pseudogap (dark gray) and superconducting gap (light gray) on the Fermi surface (heavy line).

## VII. SUMMARY AND CONCLUSIONS

Electronic Raman spectra for the cuprate systems Y123 and Bi2212 have been presented. We have studied the dependence on polarization, temperature $T$, and doping $p$. $T$ varies between 10 and 330 K and $0 < p \leqslant 0.23$ with $p = 0.16$ being the doping at the maximal $T_c$. For the analysis of the normal-state data the memory function method is adopted for the Raman case. This enables us to calculate dynamical lifetimes $\tau(\omega, T, p)$ and interaction parameters $\lambda(\omega, T, p)$ of the carriers.

In the $B_{2g}$ channel, emphasizing electronic momenta along the diagonals of the $CuO_2$ planes, we find almost quantitative agreement with ordinary transport and IR results for the dc limit and at finite frequencies, respectively. All results are consistent. The relaxation rates $\Gamma = \tau^{-1}$ do not vary significantly with $p$. At $B_{1g}$ symmetry a strong doping depen-

dence of $\Gamma(\omega,T,p)$ is observed which has not been detected previously. It is reminiscent of the strong in-plane anisotropy found with ARPES or derived from transverse charge and heat transport. However, it shows also elements of *c*-axis properties since the anisotropy between $B_{1g}$ and $B_{2g}$ symmetries is quite different in Y123 and Bi2212.

Below a characteristic temperature $T^*$ spectral weight is lost in the $B_{2g}$ spectra for energies $\hbar\omega \leqslant E^*$ where $E^* \simeq 800\ \mathrm{cm}^{-1} \simeq J$ with $J$ the magnetic exchange energy. By extrapolating the results of the dynamical response at $T > T^*$ spectra for $T < T^*$ can be synthesized and compared to those obtained experimentally. This enables us to estimate the full effect of the pseudogap on the cross section and to determine its dependence on doping and temperature. $E^*$ and the center frequency of the pseudogap neither depend on $p$ nor on $T$ in the doping range in which the pseudogap can be resolved. The gap above $T_c$ is clearly observed in the range $p \leqslant 0.20$. Its influence on the Raman spectra is less pronounced than on reflectivity measurements, a fact which might be related to the different averaging in the Fermi surface integrals and to different vertices in Raman and IR spectroscopy.

In the superconducting state pair-breaking features are observed in $B_{2g}$ symmetry at all doping levels. The spectra are indicative of a gap with $d_{x^2-y^2}$ symmetry. The characteristic energy scales with the transition temperature $T_c$ in agreement with low-energy probes such as the magnetic penetration depth or the tunneling spectra close to zero bias and, similarly as derived from Andreev reflection, is found to be close to $8k_BT_c$.

According to these results it seems more likely that the superconducting gap and the pseudogap we observe in Raman scattering are completely decoupled and that $E^*$ is almost doping independent and close to the exchange energy $J$ in agreement with IR results. $E^*$ is also the maximal energy up to which normal and SC spectra differ at optimal doping or, more physically, up to which SC correlations are effective at the highest $T_c$. The variation of the ''gaps'' on the Fermi surface is sketched in Fig. 24 for two doping levels. Close to optimal doping [Fig. 24(b)] the pseudogap is confined to a small region in **k** space; the superconducting gap is well defined all over the Fermi surface and of the same magnitude as the pseudogap. In underdoped material the pseudogap is extended over a large region in momentum space. In addition to that, the Fermi surface does apparently not exist any more [indicated by dashed lines in Fig. 24(a)]. As a consequence the superconducting gap is well defined only close to the nodes where the Fermi surface exists as well. Here, the magnitude of the gap scales with $T_c$. Probably it is not very meaningful to speak of a superconducting gap for momenta along the principal axes. This energy could rather be interpreted as the maximal binding energy of the pairs $\Delta_p$.[20]

Apparently, there are more than two energy scales in the cuprates (subject to a highly fluctuating nomenclature). The most prominent and probably best defined one is the SC gap which is sometimes also referred to as the coherence gap $\Delta_c$ and which exists only for $T < T_c$. There is increasing support for $\Delta_c \simeq 4k_BT_c$. The highest scale is set by an energy $\Delta^*$[85] or $\Delta_p$,[20,87,103] which is identified with the pseudogap or with the maximal binding energy of the electrons, respectively. They both decrease rapidly with doping and have a similar dependence on $p$. We speculate therefore that $\Delta^* \equiv \Delta_p$. In IR and Raman scattering a third almost-doping-independent energy $E^* \simeq J$ is found which becomes effective for $T < T^*$. Finally, there is a gap in the spin excitation spectrum $\Delta_{\mathrm{spin}} \simeq T^*$.[2,3,83] The relationship between the various energies is an important, so far open issue.

## ACKNOWLEDGMENTS

We gratefully acknowledge enlightening discussions with, and continuous support by, B. Stadlober, F. Venturini, K. Kamarás, D. Einzel, A. Virosztek, L. Mihaly, V. V. Moshchalkov, and A. Zawadowski. We are indebted to N. Nücker, who cut some of the postannealed crystals with the microtome. This work was supported by the Hungarian National Research Fund under Grant No. OTKA T019045. The experiments have been supported partially by the Bayerische Forschungsstiftung through the ''Forschungsverbund Hochtemperatur-Supraleiter'' (FORSUPRA). We are grateful to the BMBF for financial support via the program ''Bilaterale Wissenschaftlich-Technische Zusammenarbeit'' under Grant No. UNG-052-96.

## APPENDIX

The imaginary part of the Raman spectral function $\chi''_{\gamma\gamma}(\omega,T)$ is obtained from the rate of inelastically scattered photons $\dot{N}_{\gamma\gamma}(\omega,T)$ via Eq. (1) as

$$\chi''_{\gamma\gamma}(\omega,T) = \frac{\dot{N}_{\gamma\gamma}(\omega,T)}{R_{\gamma\gamma}\{1+n_B(\omega,T)\}}. \tag{A1}$$

As in the main part $n_B(\omega,T) = (\exp(\hbar\omega/k_BT)-1)^{-1}$ is the Bose-Einstein thermal function, the polarization (Raman vertex) indices $\gamma$ will be dropped, and a dimensionless version of the Raman spectral function $\chi$ will be used.

Since $\chi$ is a causal function with the imaginary part describing absorption processes, $\omega\chi''(\omega) \geqslant 0$ holds and $\chi''(\omega)$ decays at high energies. In the complex $z$ plane we can therefore define a holomorphic function $\chi(z)$ by the integral

$$\chi(z) = \frac{1}{\pi}\int_{-\infty}^{\infty} d\xi \frac{\chi''(\xi)}{\xi - z} \tag{A2}$$

for all nonreal $z$. Without further consequences the Raman response function $\chi(z)$ may differ by an additive constant from the Raman spectral function $\chi(\omega)$ defined as a correlation function of the effective density. The spectral function $\chi''(\omega)$ is the analytical continuation of $\chi(z)$ to the real axis,

$$\chi(\omega \pm i\delta) = \chi'(\omega) \pm i\chi''(\omega), \tag{A3}$$

and the real and imaginary parts $\chi'(\omega)$ and $\chi''(\omega)$, repectively, are related by the KK transformation

$$\chi'(\omega) = \frac{2}{\pi}\wp\int_0^{\infty} d\xi \frac{\xi\chi''(\xi)}{\xi^2 - \omega^2}, \tag{A4}$$

where $\wp$ denotes the principal value. We define now the Raman memory function $M(z)$ in an analogous way as was proposed for the conductivity by Götze and Wölfle,[33]

$$\chi(z)=\frac{M(z)}{z+M(z)}. \tag{A5}$$

Though the Raman memory function $M(z)$ is different from the conductivity memory function, its analytical properties are the same. $M(z)$ is holomorphic for all nonreal $z$ and obeys the symmetry relations $M^*(z)=M(z^*)$ and $M(z)=-M(-z)$. Therefore $M(z)$ can be represented by the spectral function $M''(\omega)$ as

$$M(z)=\frac{1}{\pi}\int_{-\infty}^{\infty}d\xi\frac{M''(\xi)}{\xi-z}, \tag{A6}$$

where $M''(\omega)$ is the analytical continuation of $M(z)$ to the real axis,

$$M(\omega\pm i\delta)=M'(\omega)\pm iM''(\omega). \tag{A7}$$

For real frequencies $\omega$ the symmetry properties of $M(z)$ imply that $M'(\omega)$ is an odd and $M''(\omega)$ is an even function of $\omega$; hence the KK relation reads

$$M'(\omega)=\frac{2\omega}{\pi}\wp\int_0^{\infty}d\xi\frac{M''(\xi)}{\xi^2-\omega^2}. \tag{A8}$$

With the usual notation $M(\omega)=\omega\lambda(\omega)+i\Gamma(\omega)$ both $\lambda(\omega)$ and $\Gamma(\omega)$ are even functions of $\omega$. $1+\lambda(\omega)=m^*/m_b$ with $m_b$ the band mass describes a frequency-dependent mass enhancement that measures the strength of the interaction of the electrons either among each other or with other excitations such as phonons. In a system of noninteracting or elastically scattered electrons $\lambda$ is identical zero. In the high-frequency limit $\lambda(\omega)$ generally approaches zero in a system of free carriers. $\Gamma(\omega)$ can be interpreted as the inverse of a frequency-dependent (Raman) relaxation time, $\Gamma(\omega)=[\tau(\omega)]^{-1}$. Of course, $\lambda(\omega)$ and $\Gamma(\omega)$ depend on temperature as well. $\lambda(\omega)$ and $\Gamma(\omega)$ are also related by KK transformations as can be seen immediately from Eq. (A8). Though formally similar the memory function $M$ should not be confused with self-energy $\Sigma$. While $M$ is a two-particle correlation function $\Sigma$ is a single-particle property in a many-body system.

At first glance the memory function $M(\omega)$ can be obtained directly from the measured Raman response $\chi''(\omega)$ by calculating the real part $\chi'(\omega)$ via the KK relation in Eq. (A4). However, the experimental spectra (see, e.g., Fig. 4) do not decay but turn out to be constant or to even increase slightly in the midinfrared range (up to a typical bandwidth of the order of 1 eV). This requires the introduction of an upper cutoff frequency $\omega_c$ in the KK integral, Eq. (A4), which turns out to influence the results seriously. In order to overcome this problem we define a new function $\overline{\chi}(z)$,

$$\overline{\chi}(z)=\frac{1}{z+M(z)}. \tag{A9}$$

Since $\chi(z)=1-z\overline{\chi}(z)$, $\overline{\chi}(z)$ and $\chi(z)$ have the same analytical behavior. For $|z|\to\infty$, $\overline{\chi}(z)$ decays as $1/z$, and can be continuated to the real axis as $\overline{\chi}(\omega\pm i\delta)=\overline{\chi}'(\omega)\pm i\overline{\chi}''(\omega)$. Obviously, $\chi'(\omega)=1-\omega\overline{\chi}'(\omega)$, $\chi''(\omega)=-\omega\overline{\chi}''(\omega)$, and $\overline{\chi}''(\omega)\leqslant 0$. Therefore $\overline{\chi}'(\omega)$ can be expressed through $\overline{\chi}''(\omega)$ as

$$\overline{\chi}'(\omega)=\frac{2\omega}{\pi}\wp\int_0^{\infty}d\xi\frac{\overline{\chi}''(\xi)}{\xi^2-\omega^2}. \tag{A10}$$

We use now the KK relation for $\chi$, Eq. (A4), but express $\chi''$ by $\overline{\chi}''$,

$$\chi'(\omega)=-\frac{2}{\pi}\wp\int_0^{\infty}d\xi\frac{\xi^2\overline{\chi}''(\xi)}{\xi^2-\omega^2}$$

$$=-\frac{2}{\pi}\wp\int_0^{\infty}d\xi\left(1+\frac{\omega^2}{\xi^2-\omega^2}\right)\overline{\chi}''(\xi).$$

This is equal to $1-\omega\overline{\chi}'(\omega)$; hence

$$1-\omega\overline{\chi}'(\omega)=-\frac{2}{\pi}\int_0^{\infty}d\xi\overline{\chi}''(\xi)-\frac{2\omega^2}{\pi}\wp\int_0^{\infty}d\xi\frac{\overline{\chi}''(\xi)}{\xi^2-\omega^2}. \tag{A11}$$

With Eq. (A10) we obtain the sum rule

$$-\frac{2}{\pi}\int_0^{\infty}d\xi\overline{\chi}''(\xi)=1. \tag{A12}$$

Whenever $\overline{\chi}''(\omega)$ decays faster than $\omega^{-1}$ the convergence is guaranteed. However, in any practical analysis a cutoff frequency $\omega_c$ has to be introduced which is typically of the order of the bandwidth. This is particularly important for Raman scattering since the cross section not only originates from carriers which the analysis is tailored for. The dependence of the integral on $\omega_c$ is crucially related to the high-energy variation of the response. It is logarithmical if $\overline{\chi}''(\omega)$ decays exactly as $\omega^{-1}$ or, equivalently, if $\chi''(\omega)$ approaches a constant value.

The advantage of the new function $\overline{\chi}$ becomes apparent when we return to the original goal, i.e., when we derive $M(\omega)$ from the Raman spectra. We start by defining a new function $I(\omega,T)=-R\overline{\chi}''(\omega,T)$ which can be expressed in terms of the measured Raman intensity $\dot{N}(\omega,T)$ as

$$I(\omega,T)=\frac{\dot{N}(\omega,T)}{\omega\{1+n_B(\omega,T)\}}. \tag{A13}$$

The sum rule, Eq. (A12), fixes the value of the scaling factor $R$,

$$\frac{2}{\pi}\int_0^{\omega_c}d\omega\, I(\omega)=R. \tag{A14}$$

Additionally, we define $K(\omega)=R\overline{\chi}'(\omega)/\omega$ and express it through the KK transform of $\overline{\chi}'(\omega)$ given in Eq. (A10),

$$K(\omega)=-\frac{2}{\pi}\wp\int_0^{\omega_c}d\xi\frac{I(\xi)}{\xi^2-\omega^2}. \tag{A15}$$

As long as $\omega \leqslant 0.2\ \omega_c$ the convergence is very fast and the dependence on $\omega_c$ correspondingly weak. By separating the real and imaginary parts we can now determine both the Raman relaxation rate $\Gamma(\omega)$ and the mass-enhancement factor $1+\lambda(\omega)$,

$$\Gamma(\omega) = R\frac{I(\omega)}{[I(\omega)]^2+[\omega K(\omega)]^2}, \tag{A16}$$

$$1+\lambda(\omega) = R\frac{K(\omega)}{[I(\omega)]^2+[\omega K(\omega)]^2}. \tag{A17}$$

We emphasize that $\omega_c$ is the only adjustable parameter and that not only the spectral shape but also the magnitude of $\Gamma$ and $1+\lambda$ is obtained. Due to the specific choice of $I(\omega)$ in Eq. (A13), the spectral shapes of $\Gamma(\omega)$ and $1+\lambda(\omega)$ become almost completely independent of $\omega_c$, and the scaling factor $R$ depends only weakly, in our case logarithmically, on the cutoff.

The above formulas are general, and the conductivity $\sigma(\omega)=\sigma'(\omega)+i\sigma''(\omega)$ can be expressed in terms of $\overline{\chi}(\omega)$,[33]

$$\sigma(\omega) = i\varepsilon_0\omega_{pl}^2\overline{\chi}(\omega), \tag{A18}$$

where $\omega_{pl}$ is the plasma frequency. If we plug that into Eq. (A12), we obtain the well-known sum rule for the real part of the conductivity,

$$\frac{2m}{\pi e^2}\int_0^\infty d\omega\,\sigma'(\omega) = n, \tag{A19}$$

with the definitions of the symbols used in Sec. V.

We can define a Raman conductivity $\sigma_{\gamma\gamma}$ by Eq. (A18) using the Raman memory function. However, due to the differences of the vertices, the optical and Raman conductivities should be considered as different quantities. Nevertheless, they display similar physical properties. The Raman conductivity in terms of the Raman intensity $I(\omega,T)$ is given by

$$\sigma_{\gamma\gamma}(\omega,T) = \varepsilon_0\omega_{pl}^2\frac{I_{\gamma\gamma}(\omega,T)+i\omega K_{\gamma\gamma}(\omega,T)}{R_{\gamma\gamma}}, \tag{A20}$$

where $R_{\gamma\gamma}=R_{\gamma\gamma}(\omega_c,T)$ in the general case. $\sigma_{\gamma\gamma}$ depends on the polarizations and reflects therefore **k** dependent properties.


[1] K.B. Lyons, P.A. Fleury, L.F. Schneemeyer, and J.V. Waszczak, Phys. Rev. Lett. **60**, 732 (1988); K.B. Lyons and P.A. Fleury, J. Appl. Phys. **64**, 6075 (1988).

[2] M. Takigawa, A.P. Reyes, P.C. Hammel, J.D. Thompson, R.H. Heffner, Z. Fisk, and K.C. Ott, Phys. Rev. B **43**, 247 (1991); see also, A.J. Millis, H. Monien, and D. Pines, *ibid.* **42**, 167 (1990).

[3] P. Bourges, L.P. Regnault, Y. Sidis, and C. Vettier, Phys. Rev. B **53**, 876 (1996).

[4] D. Pines, Z. Phys. B: Condens. Matter **103**, 129 (1997), and references therein.

[5] J.W. Loram, K.A. Mirza, J.R. Cooper, and W.Y. Liang, Phys. Rev. Lett. **71**, 1740 (1993).

[6] C.C. Homes, T. Timusk, R. Liang, D.A. Bonn, and W.N. Hardy, Phys. Rev. Lett. **71**, 1645 (1993); S. Uchida, K. Tamasaku, K. Takenaka, and Y. Fukuzumi, J. Low Temp. Phys. **105**, 723 (1996), and references therein.

[7] A.V. Puchkov, P. Fournier, D.N. Basov, T. Timusk, A. Kapitulnik, and N.N. Kolesnikov, Phys. Rev. Lett. **77**, 3212 (1996).

[8] R. Nemetschek, M. Opel, C. Hoffmann, P.F. Müller, R. Hackl, H. Berger, L. Forró, A. Erb, and E. Walker, Phys. Rev. Lett. **78**, 4837 (1997).

[9] M. Opel, R. Nemetschek, C. Hoffmann, P.F. Müller, R. Philipp, R. Hackl, H. Berger, L. Forró, A. Erb, and E. Walker, J. Phys. Chem. Solids **59**, 1942 (1998).

[10] C. Renner, B. Revaz, J.-Y. Genoud, K. Kadowaki, and Ø. Fischer, Phys. Rev. Lett. **80**, 149 (1998).

[11] C. Renner, B. Revaz, K. Kadowaki, I. Maggio-Aprile, and Ø. Fischer, Phys. Rev. Lett. **80**, 3606 (1998).

[12] K. Ishida, K. Yoshida, T. Mito, Y. Tokunaga, Y. Kitaoka, K. Asayama, Y. Nakayama, J. Shimoyama, and K. Kishio, Phys. Rev. B **58**, R5960 (1998).

[13] For a review, see T. Timusk and B.W. Statt, Rep. Prog. Phys. **62**, 61 (1999).

[14] V.J. Emery and S.A. Kivelson, Nature (London) **374**, 434 (1995).

[15] A.M. Cucolo, M. Cuoco, and A.A. Varlamov, Phys. Rev. B **59**, R11 675 (1999), and references therein.

[16] A.S. Alexandrov and N.F. Mott, *Polarons and Bipolarons* (World Scientific, Singapore, 1996).

[17] J. Ranninger and A. Romano, Phys. Rev. Lett. **80**, 5643 (1998), and references therein.

[18] A.G. Loeser, Z.-X. Shen, D.S. Dessau, D.S. Marshall, C.H. Park, P. Fournier, and A. Kapitulnik, Science **273**, 325 (1996).

[19] H. Ding, T. Yokoya, J.C. Campuzano, T. Takahashi, M. Randeria, M.R. Norman, T. Mochiku, K. Kadowaki, and J. Giapinzakis, Nature (London) **382**, 51 (1996).

[20] G. Deutscher, Nature (London) **397**, 410 (1999).

[21] H. Ding, M.R. Norman, T. Yokoya, T. Takeuchi, M. Randeria, J.C. Campuzano, T. Takahashi, T. Mochiku, and K. Kadowaki, Phys. Rev. Lett. **78**, 2628 (1997).

[22] T. Staufer, R. Hackl, and P. Müller, Solid State Commun. **75**, 975 (1990); **79**, 409 (1991).

[23] R. Hackl, M. Opel, P.F. Müller, G. Krug, B. Stadlober, R. Nemetschek, H. Berger, and L. Forró, J. Low Temp. Phys. **105**, 733 (1996).

[24] B.P. Stojković and D. Pines, Phys. Rev. Lett. **76**, 811 (1996); Phys. Rev. B **55**, 8576 (1997).

[25] T.P. Devereaux and A.P. Kampf, Phys. Rev. B **59**, 6411 (1999).

[26] For a review and for references, see E. Dagotto, Rev. Mod. Phys. **66**, 763 (1994); H. Fukuyama and H. Kohno, Czech. J. Phys. **46**, 3146 (1996); P.A. Lee, J. Low Temp. Phys. **105**, 581 (1996); Physica C **317-318,** 194 (1999).

[27] F.C. Zhang and T.M. Rice, Phys. Rev. B **37**, 3759 (1988).

[28] D.J. Scalapino, Phys. Rep. **250**, 329 (1995).

[29] G. Dopf, A. Muramatsu, and W. Hanke, Physica C **185-189**, 1495 (1991); J. Wagner, W. Hanke, and D.J. Scalapino, *ibid.* **185-189**, 1617 (1991); Phys. Rev. B **43**, 10 517 (1991).

[30] A. Virosztek and J. Ruvalds, Phys. Rev. B **45**, 347 (1992).

[31] A. Zawadowski and M. Cardona, Phys. Rev. B **42**, 10 732 (1990).

[32] D.B. Tanner and T. Timusk, in *Physical Properties of High Temperature Superconductors III*, edited by D.M. Ginsberg (World Scientific, Singapore, 1992), p. 363.
[33] W. Götze and P. Wölfle, Phys. Rev. B **6**, 1226 (1972).
[34] T.P. Devereaux and D. Einzel, Phys. Rev. B **51**, 16 336 (1995); **54**, 15 547 (1996).
[35] M.R. Norman, H. Ding, H. Fretwell, M. Randeria, and J.C. Campuzano, Phys. Rev. B **60**, 7585 (1999).
[36] T.P. Devereaux, D. Einzel, B. Stadlober, R. Hackl, D.H. Leach, and J.J. Neumeier, Phys. Rev. Lett. **72**, 396 (1994); **72**, 3291 (1994).
[37] D. Einzel and R. Hackl, J. Raman Spectrosc. **27**, 307 (1996).
[38] R. Hackl, in *The Gap Symmetry and Fluctuations in High-$T_c$ Superconductors*, Vol. 371 of *NATO Advanced Study Institute, Series B: Physics*, edited by J. Bok, G. Deutscher, D. Pavuna, and S. Wolf (Plenum, New York, 1998), pp. 255–296.
[39] F. Slakey, M.V. Klein, J.P. Rice, and D.M. Ginsberg, Phys. Rev. B **43**, 3764 (1991).
[40] A. Erb, E. Walker, and R. Flükiger, Physica C **258**, 9 (1996).
[41] A. Erb, E. Walker, J.-Y. Genoud, and R. Flükiger, Physica C **282-287**, 89 (1997).
[42] T.B. Lindemer, J.F. Hunley, J.E. Gates, A.L. Sutton, J. Brynestad, C.R. Hubbard, and P.K. Gallagher, J. Am. Ceram. Soc. **72**, 1775 (1989).
[43] R. Feile, Physica C **159**, 1 (1989).
[44] E. Osquiguil, M. Maenhoudt, B. Wuyts, Y. Bruynseraede, D. Lederman, and I.K. Schuller, Phys. Rev. B **49**, 3675 (1994).
[45] M.R. Presland, J.L. Tallon, R.G. Buckley, R.S. Liu, and N.E. Flower, Physica C **176**, 95 (1991); J.L. Tallon, C. Bernhard, H. Shaked, R.L. Hitterman, and J.D. Jørgensen, Phys. Rev. B **51**, 12 911 (1995).
[46] R.E. Gladyshevskii and R. Flükiger, Acta Crystallogr., Sect. B: Struct. Sci. **52**, 38 (1996).
[47] B. Revaz (private communication).
[48] H. Berger (private communication).
[49] A. Zibold, L. Widder, H.P. Geserich, G. Bräuchle, H. Claus, H. v. Löhneysen, N. Nücker, A. Erb, and G. Müller-Vogt, Physica C **1212**, 365 (1993).
[50] P.E. Sulewski, P.A. Fleury, K.B. Lyons, and S.-W. Cheong, Phys. Rev. Lett. **67**, 3864 (1991).
[51] D. Salamon, R. Liu, M.V. Klein, M.A. Karlow, S.L. Cooper, S.-W. Cheong, W.C. Lee, and D.M. Ginsberg, Phys. Rev. B **51**, 6617 (1995).
[52] C. Thomsen and M. Cardona, in *Physical Properties of High Temperature Superconductors I*, edited by D.M. Ginsberg (World Scientific, Singapore, 1989), p. 509; C. Thomsen, in *Light Scattering in Solids VI*, Topics in Applied Physics Vol. 68 (Springer, Berlin, 1991), p. 285.
[53] R. Nemetschek, R. Hackl, M. Opel, R. Philipp, M.T. Béal-Monod, J.B. Bieri, K. Maki, A. Erb, and E. Walker, Eur. Phys. J. B **5**, 495 (1998).
[54] T. Katsufuji, Y. Tokura, T. Ido, and S. Uchida, Phys. Rev. B **48**, 16 131 (1993).
[55] X.-K. Chen, J.G. Naeini, K.C. Hewitt, J.C. Irwin, R. Liang, and W.N. Hardy, Phys. Rev. B **56**, R513 (1997).
[56] J.G. Naeini, X.-K. Chen, J.C. Irwin, M. Okuya, T. Kimura, and K. Kishio, Phys. Rev. B **59**, 9642 (1999).
[57] M. Pressl, M. Mayer, P. Knoll, S. Lo, U. Hohenester, and E. Holzinger-Schweiger, J. Raman Spectrosc. **27**, 343 (1996).
[58] M. Rübhausen, N. Dieckmann, A. Bock, U. Merkt, W. Widder, and H.F. Braun, J. Low Temp. Phys. **105**, 761 (1996).
[59] D. Reznik, S.L. Cooper, M.V. Klein, W.C. Lee, D.M. Ginsberg, A.A. Maksimov, A.V. Puchkov, I.I. Tartakovskii, and S.-W. Cheong, Phys. Rev. B **48**, 7624 (1993).
[60] A.A. Abrikosov and V.M. Genkin, Zh. Éksp. Teor. Fiz. **65**, 842 (1973) [Sov. Phys. JETP **38**, 417 (1974)]; M.V. Klein and S.B. Dierker, Phys. Rev. B **29**, 4976 (1984).
[61] The characteristic temperature $T^*$ can be determined directly from the Raman spectra either by simply comparing results taken at different temperatures or by calculating the integral over the cross section (Refs. 8 and 62). In all cases we identified the onset of the changes with $T^*$. The results are consistent to within approximately 30 K.
[62] M. Opel, M. Götzinger, C. Hoffmann, R. Nemetschek, R. Philipp, F. Venturini, R. Hackl, A. Erb, and E. Walker, J. Low Temp. Phys. **117**, 347 (1999).
[63] A. Erb, J.-Y. Genoud, F. Marti, M. Däumling, E. Walker, and R. Flükiger, J. Low Temp. Phys. **105**, 1023 (1996).
[64] T.P. Devereaux, Phys. Rev. Lett. **74**, 4313 (1995).
[65] M. Opel, R. Nemetschek, F. Venturini, R. Hackl, A. Erb, E. Walker, H. Berger, and L. Forró, Phys. Status Solidi B **215**, 417 (1999).
[66] R. Nemetschek, Ph.D. thesis, Technical University Munich (Hieronymus, München, 1998).
[67] After completion of this manuscript we received a paper before publication by Naeini *et al.*, where a similar way of analysis is proposed and applied to LSCO. The present paper goes a little beyond that, and we derive here a virtually parameter-free formalism for the determination of $\Gamma(\omega,T)$ and $1+\lambda(\omega,T)$ which yields not only the spectral shape but also the magnitude of the quantities. Those experimental data which can be compared are in full agreement.
[68] M. Tinkham, *Introduction to Superconductiviy* (McGraw-Hill, Tokyo, 1975).
[69] D. Einzel and C. Schuster, Czech. J. Phys. **46**, 993 (1996).
[70] B. Stadlober, G. Krug, R. Nemetschek, M. Opel, R. Hackl, D. Einzel, C. Schuster, T.P. Devereaux, L. Forró, J.L. Cobb, J.T. Markert, and J.J. Neumeier, J. Phys. Chem. Solids **56**, 1841 (1995).
[71] T. Ito, K. Takenaka, and S. Uchida, Phys. Rev. Lett. **70**, 3995 (1993).
[72] C. Kendziora, M.C. Martin, J. Hartge, L. Mihaly, and L. Forró, Phys. Rev. B **48**, 3531 (1993).
[73] D.B. Romero, C.D. Porter, D.B. Tanner, L. Forró, D. Mandrus, L. Mihaly, G.L. Carr, and G.P. Williams, Solid State Commun. **82**, 183 (1992).
[74] J. Orenstein, G.A. Thomas, A.J. Millis, S.L. Cooper, D.H. Rapkine, T. Timusk, L.F. Schneemayer, and J.V. Wazczak, Phys. Rev. B **42**, 6342 (1990).
[75] T.R. Chien, Z.Z. Wang, and N.P. Ong, Phys. Rev. Lett. **67**, 2088 (1991).
[76] A. Carrington, A.P. Mackenzie, C.T. Lin, and J.R. Cooper, Phys. Rev. Lett. **69**, 2855 (1992).
[77] C. Kendziora, D. Mandrus, L. Mihaly, and L. Forró, Phys. Rev. B **46**, 14 297 (1992).
[78] B. Zeini, A. Freimuth, B. Büchner, R. Gross, A.P. Kampf, M. Kläser, and G. Müller-Vogt, Phys. Rev. Lett. **82**, 2175 (1999).
[79] L. Forró, Phys. Lett. A **179**, 140 (1993).
[80] P.W. Anderson, Phys. Rev. Lett. **67**, 2092 (1991).
[81] P.A. Fleury and R. Loudon, Phys. Rev. **166**, 514 (1968).
[82] M.R. Norman, M. Randeria, H. Ding, and J.C. Campuzano, Phys. Rev. B **57**, R11 093 (1998).

[83] V.V. Moshchalkov, L. Trappeniers, and J. Vanacken, Europhys. Lett. **46**, 75 (1999).
[84] I. Vobornik, H. Berger, D. Pavuna, M. Onellion, G. Margaritondo, F. Rullier-Albenque, L. Forró, and M. Grioni, Phys. Rev. Lett. **82**, 3128 (1999).
[85] H. Ding, J.C. Campuzano, M.R. Norman, M. Randeira, T. Yokoya, T. Takahashi, T. Takeuchi, T. Mochiku, K. Kadowaki, P. Guptasarma, and D.G. Hinks, J. Phys. Chem. Solids **59**, 1888 (1998).
[86] J. Halbritter, J. Supercond. **11**, 231 (1998).
[87] D. Mihailovic, B. Podobnik, J. Demsar, G. Wagner, and J. Evetts, J. Phys. Chem. Solids **59**, 1937 (1998); J. Demsar, B. Podobnik, V.V. Kabanov, T. Wolf, and D. Mihailovic, Phys. Rev. Lett. **82**, 4918 (1999); V.V. Kabanov, J. Demsar, B. Podobnik, and D. Mihailovic, Phys. Rev. B **59**, 1497 (1999).
[88] J.R. Engelbrecht, A. Nazarenko, M. Randeria, and E. Dagotto, Phys. Rev. B **57**, 13 406 (1998).
[89] N. Furukawa, T.M. Rice, and M. Salmhofer, Phys. Rev. Lett. **81**, 3195 (1998).
[90] J. Schmalian, D. Pines, and B. Stojković, Phys. Rev. Lett. **80**, 3839 (1998).
[91] J. Schmalian, D. Pines, and B. Stojković, Phys. Rev. B **60**, 667 (1999).
[92] A.A. Abrikosov and L.A. Fal'kovskii, Zh. Éksp. Teor. Fiz. **40**, 262 (1961) [Sov. Phys. JETP **13**, 179 (1961)].
[93] X.-K. Chen, J.C. Irwin, H.J. Trohdal, T. Kimura, and K. Kishio, Phys. Rev. Lett. **73**, 3290 (1994).
[94] L.V. Gasparov, P. Lemmens, N.N. Kolesnikov, and G. Güntherodt, Phys. Rev. B **58**, 11 753 (1998).
[95] C. Kendziora and A. Rosenberg, Phys. Rev. B **52**, R9867 (1995).
[96] C. Kendziora, R.J. Kelley, and M. Onellion, Phys. Rev. Lett. **77**, 727 (1996).
[97] R. Hackl, G. Krug, R. Nemetschek, M. Opel, and B. Stadlober, Proc. SPIE **2696**, 194 (1996).
[98] A. Bock, Ann. Phys. (Leipzig) **8**, 441 (1999).
[99] The existence of $B_{2g}$ pair-breaking features and, sometimes, even the existence of $B_{2g}$ intensity at all is still not generally accepted but there is also confirmation from other groups for optimally doped samples (Refs. 94 and 100) and underdoped material (Refs. 55 and 56). Here we can safely exclude that polarization leakage gives rise to the $B_{2g}$ spectra. The small peak in the $B_{2g}$ spectra at 340 $cm^{-1}$ (see, e.g., Fig. 7) is indeed due to leakage of a $B_{1g}$ phonon coming from the twinning of the crystals. Its effect can be estimated to be approximately 1%. However, 1% of the electronic $B_{1g}$ intensity would be 0.01 counts per second and this is indeed unobservable.
[100] M.C. Krantz and M. Cardona, Phys. Rev. Lett. **72**, 3290 (1994).
[101] G. Blumberg, M. Kang, M.V. Klein, K. Kadowaki, and C. Kendziora, Science **278**, 1427 (1997).
[102] M.R. Norman, H. Ding, M. Randeria, J.C. Campuzano, T. Tokoya, T. Takeuchi, T. Takahashi, T. Mochiku, K. Kadowaki, P. Guptasarma, and D.G. Hinks, Nature (London) **392**, 157 (1998).
[103] N. Miyakawa, P. Guptasarma, J.F. Zasadzinski, D.G. Hinks, and K.E. Gray, Phys. Rev. Lett. **80**, 157 (1998).
[104] C. Panagopoulos and T. Xiang, Phys. Rev. Lett. **81**, 2336 (1998).